Kanninen, Pekka; Peltonen, Petteri; Vuorinen, Ville

Full-scale ship stern wave with the modelled and resolved turbulence including the hull roughness effect

Published in:
Ocean Engineering

DOI:
10.1016/j.oceaneng.2021.110434

Published: 01/02/2022

Document Version
Peer-reviewed accepted author manuscript, also known as Final accepted manuscript or Post-print

Full-scale ship stern wave with the modelled and resolved turbulence including the hull roughness effect

Pekka Kanninen[a,*], Petteri Peltonen[b], Ville Vuorinen[c]

[a] *Meyer Turku, P.O. Box 666, Telakkakatu 1, FI-20101 Turku, Finland*
[b] *Technical Research Centre of Finland, FI-02044 VTT, Finland*
[c] *Aalto University, Department of Mechanical Engineering, FI-00076 Aalto, Finland*

Abstract

Stern wave flow phenomena are investigated in a full-scale Kriso container ship. The hull roughness effects are studied with and without propulsion. Reynolds-averaged Navier-Stokes (RANS) and detached eddy simulations (DES) are utilized with the ghost-fluid method (GFM). The DES is carried out with a submodel where a stationary RANS solution is used as a boundary condition. The surface roughness effect on the stern is significant due to the increased boundary layer thickness. The differences in the stern wave shape between RANS and DES become more pronounced with propulsion as DES resolves the turbulence and wave breaking. With the smooth hull, DES indicates transom wetting which RANS does not. For the heavy fouling condition RANS and DES predict a wetted transom. For the smooth hull, the DES results indicate 6.8 % higher pressure (2.8% in total) resistance at the transom compared to the corresponding RANS. The resistance of the wetted transom correlates with the velocity change at the transom location. Heavy fouling does not cause pressure resistance although RANS and DES predict a wetted transom. We propose that the increased boundary layer should be taken into account in the after body design.

Keywords: CFD, Ghost fluid method, Ship scale, Transom flow, Hull roughness, DES

*Corresponding author
pekka.kanninen@meyerturku.fi

1. Introduction

To achieve a good energy efficiency, a reliable method to predict ship resistance and propulsion power is essential. Model tests are still a widely used method to make such predictions but nowadays CFD has become more common to replace some model experiments. Predictive CFD methods have been already developed using experimental data on model-scale ships. However, in both approaches, there is still uncertainty regarding the scale effects. In order to avoid scaling uncertainty, the calculation can be done in the ship scale. Validation of ship scale results is considerably more difficult because the sea trial results give the archived speed and needed power, which are an end result of the hull resistance, propulsion factors and interaction on the hull. The performance values also include a correction of test weather and loading conditions. The surface roughness of the hull creates significant uncertainty for the determination and modeling of which there is no established practice [1].

A full-scale CFD validation is presented in [2] where correction data from nine bulk carriers sea trials from the same series are used. Authors report that roughness causes approximately a 7 % effect to the propulsion power. There is no mentioning of it being caused by the antifouling coating only or whether also some fouling has happened.

By taking some numbers from the blind simulation work shop submission it is possible to note that the deviation from the reference data is higher for the full-scale data as compared to the model-scale. For example, in the model-scale resistance the mean value error is 0.1 % and standard deviation (STD) 2.1 % [3], respectively in the full-scale STD it is 9 % [4]. The propulsion coefficient STD is higher in both scales.

One way to develop the reliability of the full-scale simulation is to isolate the phenomena where there is known to be a lack in accuracy. Known limitations of the Reynolds-averaged Navier-Stokes (RANS) solution accuracy are related to the modelled turbulence and boundary layer. Ship scale CFD simulation is mainly carried out by RANS based solution by modelled boundary layer due to the $Re \sim 1 \times 10^9$ level. Such a bottle-neck largely limits usage of Large Eddy Simulation (LES) at present. Higher computational resources enable transition towards scale-resolved turbulence simulations under certain limitations. An example of a phenomenon which is not well captured using RANS method is breaking of a wave.

The Froude hypothesis assumes the ship residual resistance to be scale-

independent (see e.g. [5]). Baba [6] compared the hull resistance experimentally using the parabolic Wigley hull and a tanker hull with a transom stern. The study presents the resistance component of a breaking wave which is missing in the original Froude's hypothesis. In contrast to the Froude hypothesis, it is known that a breaking wave occurs behind the transom generating a Reynolds number dependent resistance component [7, 8].

The breaking wave can cause an error to the ship resistance prediction when the model test [9] or RANS simulation is used [7]. The stern wave breaking and resistance effect has been investigated with a vessel which has a wide immersed transom stern [10, 11]. Authors discussed the forward oriented breaking waves which influence the resistance and have scale effects. However, the authors carried out towing model tests on different scales i.e. propulsion is not taken into account.

Duy et al. [12] carried out a stern shape optimization study for the KRISO Container Ship (KCS). The authors studied two different hull breaths and three transom shapes comparing the results to the orginal hull geometry. The starting point to optimization work is the transom configuration effect to flow fields behind the ship. The authors raised concerns on the ability of the model to capture the turbulent wake and the hull-propeller interaction. The study was conducted using RANS on model-scale.

The effect of fouling and surface roughness on the KCS resistance has been studied by multiple authors. Demirel et al. [13] considered the effect of biofouling for the full-scale KCS with six different surface roughness conditions and compared the results to a smooth hull simulation. One of the key findings by Demirel et al. is the decreasing wave resistance with an increasing surface roughness. The authors report about 30% reduction in the stern wave height when a calcareous fouling conditions are compared to smooth hull results. A similar trend has also been reported by Song et al. [14]. The study by Song et al. considers the KCS and the Moeri tanker (KVLCC2) in two model-scales (1:58 and 1:10) and in full-scale using RANS. In the study the residual resistance C_R is defined by the free surface simulation. Respectively, the double-body simulations where the free surfaces are replaced with the symmetry boundary condition is used to define the wave resistance $C_W = C_R - kC_F$ by using the form factor $(1 + k) = C_T/C_F$ (total resistance ratio to frictional resistance). Song et al. [14] consider smooth conditions as well as three different roughness levels. The effect of biofouling on the propulsion power requirement has been studied by Degiuli et al. [15]. The authors report that fouling increases the boundary layer thickness which affects the

propeller wake and the forming stern wave of the KCS and KVLCC2.

The motivation to use computationally demanding Detached Eddy Simulation (DES) for ship hydrodynamics simulation is related mainly to resolving flow separation, complex flow structures [16, 17] and the breaking wave phenomena [18]. Pattenden et al. and Carrica et al. utilized DES in the model-scale and Yin et al. [19] in the full-scale. Wang et al. [18] compare unsteady RANS and delayed DES method capability to capture breaking bow wave by KCS with the high Froude numbers 0.35 and 0.4. The authors report a similar resistance value by both methods at Froude number 0.26. In the higher Froude number (speed) URANS case the vorticity dissipates faster when compared to DDES causing a difference to the breaking bow wave.

OpenFOAM validation with Spalart-Allmaras (S-A) turbulence model in a 3D wake field has been previously shown by Boudreau et al. [20]. They compare unsteady RANS and DDES simulation data to experimental data for a square cylinder case at Reynolds number 21400. The study investigates velocity recovery in the wake field and flow fluctuation. The authors claim that the DDES results pose more realistic 3D features and agreement on the experimental data is clearly better when compared to the URANS equivalent. The authors also recommended DDES modeling for reliable wake prediction.

A more complex bluff-body wake study is presented by Yuan et al. [21]. The study includes ship air wake experiments and simulations using OpenFOAM and S-A-DDES model. The study shows that the computed results are in reasonable agreement with the wind tunnel data. Analysis shows that the model can capture unsteady flow field features. Based on the previous studies, we can conclude that the DES solution in the wake simulation can be considered to be more accurate than URANS simulation because the flow is better resolved.

Based on earlier studies by the present authors [8] and Yamano et al. [11] the stern wave formation depends on the boundary layer thickness at the stern. Since the boundary layer thickness depends [22] on the surface roughness, it can be assumed that the effect of surface roughness on the hull total resistance is two-fold. Firstly, the surface roughness increases the viscous drag throughout the wetted area of the hull. Secondly, the surface roughness changes the flow field next to the hull which results in changes in the Kelvin wave pattern. Figure 1 illustrates the distribution of pressure, friction and total resistance on the smooth KCS surface. As can be seen from the figure, pressure resistance is the sum of high drag in the bow and a pushing component on the stern and contributes approximately to 30% of the total re-

sistance. Here, we focus on how the surface roughness affects the distribution of the resistance components for the full-scale KCS in towed and propulsion conditions. The objectives of the present paper are related to full-scale KCS hull investigations and listed as follows.

- Quantify how the surface roughness affects the boundary layer thickness and the resistance components in towed and propulsion conditions.
- Understand the differences between RANS (turbulence modeled) and DES (turbulence resolved) approaches.

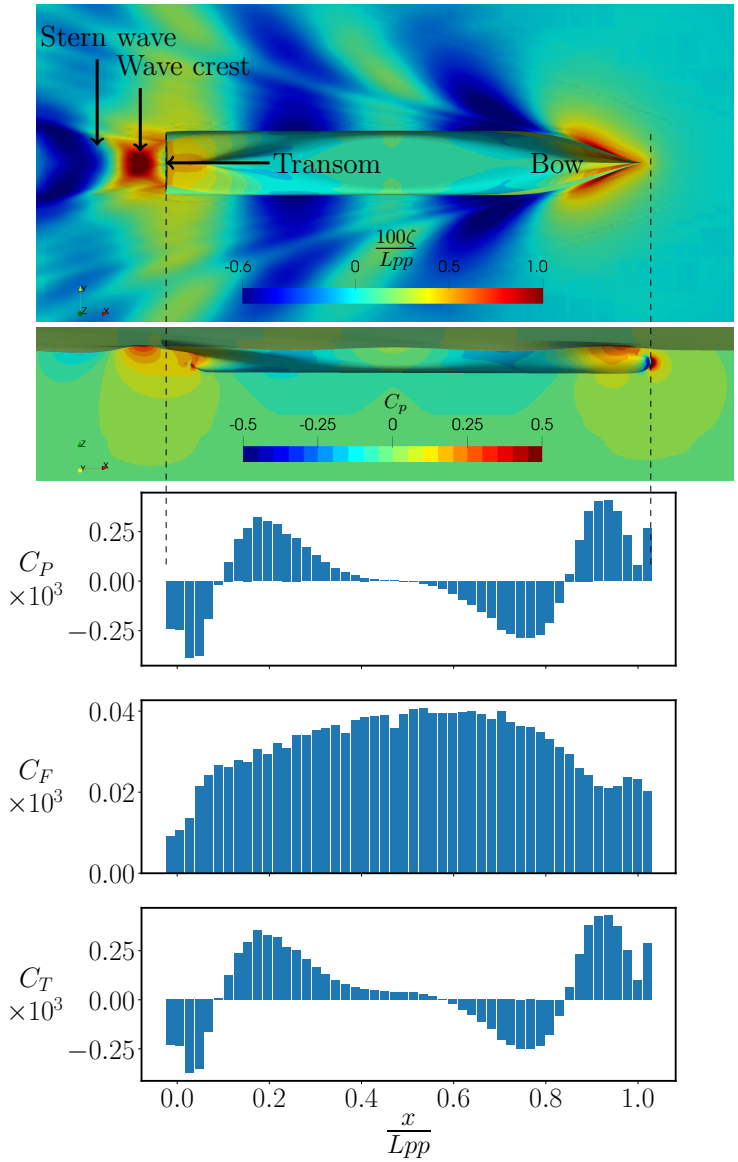

Figure 1: Typical Kelvin wave pattern and pressure distribution on a ship hull using RANS modeling. Top: Wave elevation ζ and contour plot of $C_p = \frac{2p_d}{\rho U^2}$ in the hull surface and middle section. Rest: Histogram plots of resistance coefficient $C = \frac{2F_x}{\rho S U^2}$ with pressure P, friction F and total T hull resistance force x-component F_x. Resistance force calculated from dynamic pressure p_d.

2. Methods

2.1. Studied cases

In the present study the KCS is studied with varying surface roughness as well as with and without propulsion. Furthermore, we apply both RANS and DES methods. For practical reasons, the DES is applied only to the stern part of the ship using a submodel approach. The purpose of the DES simulations is to verify the observations in the RANS simulations. All simulations are carried out for the full-scale ship and the main features of the KCS are presented in Table 1. We note that the rudder is not included in the ship model. Moreover, to reduce the computational cost symmetry is applied in DES cases where propulsion effects are not studied. All simulations are carried out with a ship speed of $U_s = 24$ kn corresponding to a Froude number $Fn = U_s/\sqrt{gLwl} = 0.26$ and Reynolds number $Re = U_s Lwl/\nu = 2.41 \times 10^9$. The full list of simulations is presented in Table 2.

Table 1: Main particulars of KCS [23, 24].

Lpp	230	m
Lwl	232.5	m
B	32.2	m
T	10.8	m
∇	52030	m^3
S w/o rudder	9424	m^2
LCB	111.6	m

Table 2: The studied cases. When propulsion effects are studied, the ID of the case is extended with P. For instance S-P corresponds to the smooth simulation with propulsion.

ID	Propulsion	Surface roughness	Method	Full ship	Purpose
		k_G μm			
S	Yes	0	RANS	Yes	Baseline
R1	Yes	2.59	RANS	Yes	Surface roughness effects
R2	Yes	24	RANS	Yes	Surface roughness effects
R3	Yes	489	RANS	Yes	Surface roughness effects
R4	Yes	3580	RANS	Yes	Surface roughness effects
S-DES	Yes	0	DES	Submodel	Validation
R4-DES	No	3580	DES	Submodel	Surface roughness validation

The computational domain size is $5 \times Lpp$ in the streamwise, $3 \times B$ in the beam and $2 \times Lpp$ in the vertical directions. The domain is discretized by using an unstructured mesh consisting mainly of hexahedral cells and the used mesh resolution is shown in Table 3. In the DES cases a uniform node distribution ($\Delta_x \approx \Delta_y \approx \Delta_z$) mesh is used and in the boundary layer the maximum aspect ratio is at level 20, see bottom Figure 2. At the transom location the actual boundary layer thickness δ ratio to discretization spacing Δ is $\delta/\Delta \approx 22$ in the medium mesh case. Such a fine mesh resolution could also correspond to a wall-modelled LES [25]. The mesh convergence result with DES method is shown in Figure 2.

Table 3: Details of the used meshes in the KCS. N_{bl} stands for the number of body-fitted boundary layer cells in the wall normal direction. Note that N_{total} in DES indicates the cell count for half hull due to symmetry.

case	$N_{total} \times 10^6$	N_{bl}	δy^+
S, R1 - R4	14.2	24	448
DES-coarse	16	15	762
DES-medium	27	15	762
DES-dense	46	15	762

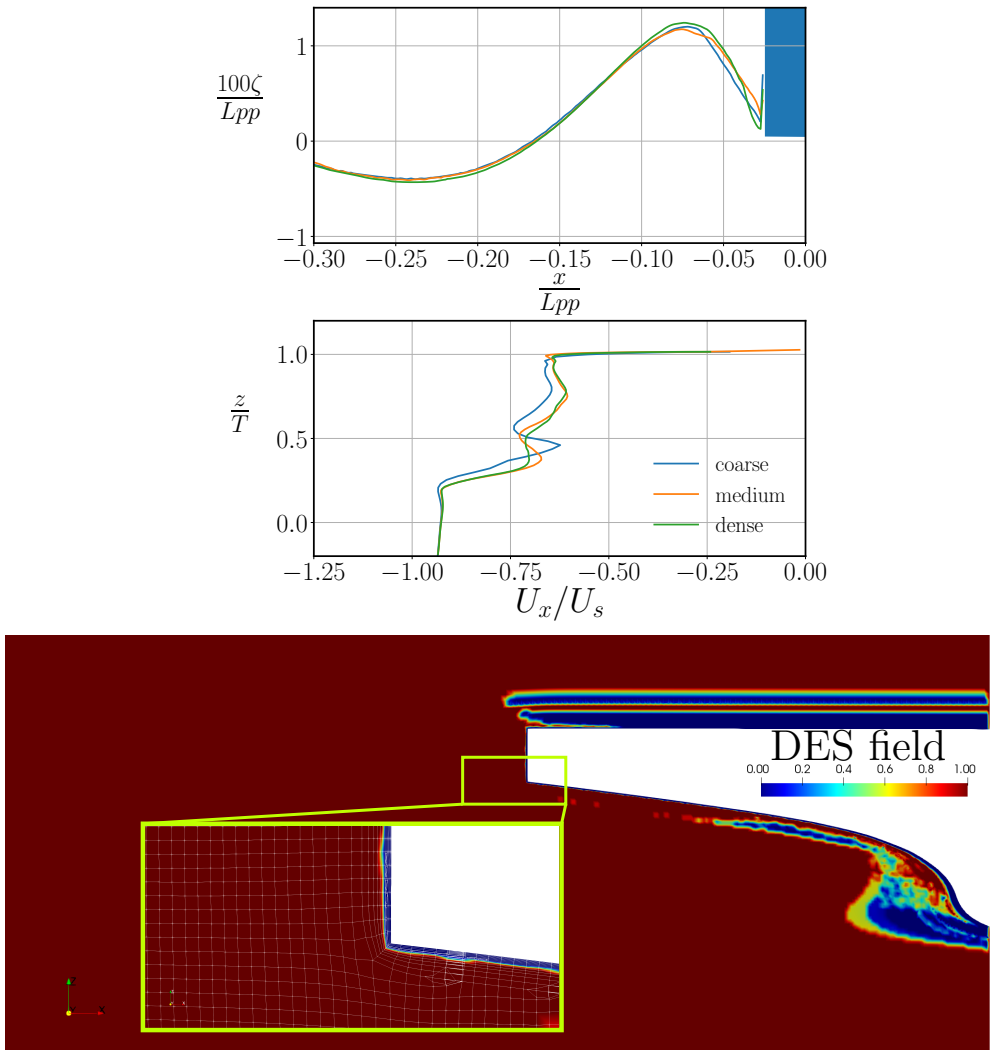

Figure 2: Top: The wave elevation ζ and the streamwise velocity profiles taken from the transom corner in the DES simulations computed with three different grid resolutions. Bottom: DES-zone in the medium grid simulation, with red DES and with blue RANS zone. The medium grid is chosen in the study.

2.2. Numerical approach

2.2.1. Governing equations

The two-phase flow is assumed to be incompressible and immiscible with negligible surface tension. The flow is governed by the mass

$$\nabla \cdot \vec{u} = 0 \tag{1}$$

and momentum

$$\frac{\partial \vec{u}}{\partial t} + \nabla \cdot (\vec{u}\vec{u}) - \beta \nabla \cdot \left(\mu(\nabla \vec{u} + \nabla \vec{u}^T)\right) = -\beta \nabla p_d \tag{2}$$

conservation equations. In Eq. 1 and 2 $\vec{u}$ is the velocity, μ is the dynamic viscosity, p_d is the dynamic pressure ($p_d = p - \rho \vec{g} \cdot \vec{x}$) and β is the inverse density of either liquid $1/\rho_L$ or gas $1/\rho_G$. The governing equations are solved with the volume of fluid (VOF) based ghost-fluid method (GFM) implemented [26] by the authors to the OpenFOAM-v2006 CFD-library [27]. The transport equation for the water volume fraction α reads

$$\frac{\partial \alpha}{\partial t} + \nabla \cdot (\alpha \vec{u}) = 0. \tag{3}$$

Eq. 3 is solved with the MULES [28] algorithm. We note that the present implementation of the GFM follows that of Vukčević et al. [29] with the exception of the definition of the interface location between adjacent cell centers. More details on the interface location definition are provided in section 2.2.2. The RANS simulations are carried out with the SST $k-\omega$ [30] turbulence model while the DES simulations are carried out with the Spalart-Allmaras (S-A) delayed DES [25] model readily available in OpenFOAM. Another possibility would be to choose SST $k-\omega$ DES model, but in the literature it is possible to find more test cases using the S-A model. This is the main reason to choose the S-A model.

2.2.2. Improved GFM interface location

In the present GFM, the interface location between adjacent interface cells P and N is defined as

$$\vec{x}_\Gamma = \vec{x}_P + \lambda \vec{d}, \tag{4}$$

where $\vec{x}_P$ is the location of cell center P and $\vec{d}$ is a vector from P to N and λ is a weighting parameter depending on the volume fractions. Here, a cell pair contains an interface if either P or N is wet ($\alpha \geq 0.5$) and the neighbour is dry ($\alpha < 0.5$).

Vukčević et al. [29] proposed defining λ as

$$\lambda = \frac{\alpha_P - 0.5}{\alpha_P - \alpha_N}, \tag{5}$$

where the subscripts denote the volume fractions in cells P and N. However, the definition in Eq. 5 causes an inadequate propagation of the wave tip in the Kelvin wave pattern [26]. Therefore, an alternative formulation for λ is proposed herein. The new λ definition reads

$$\lambda = \begin{cases} \alpha_P + \alpha_N - 0.5 & \alpha_P \geq 0.5 \\ 1.5 - (\alpha_P + \alpha_N) & \alpha_P < 0.5. \end{cases} \tag{6}$$

A contour plot highlighting the difference between the two λ definitions is presented in Figure 3 with different α values. The benefit of using Eq. 6 is highlighted in cases where the wet cell volume fraction is only slightly above 0.5 and change of the dry cell volume fraction causes moderate change in λ i.e. volume fraction correlation to λ is linear. In practice, using Eq. 6 overcomes the inadequate propagation of the small amplitude waves as illustrated in Figure 4 for the KCS wave pattern.

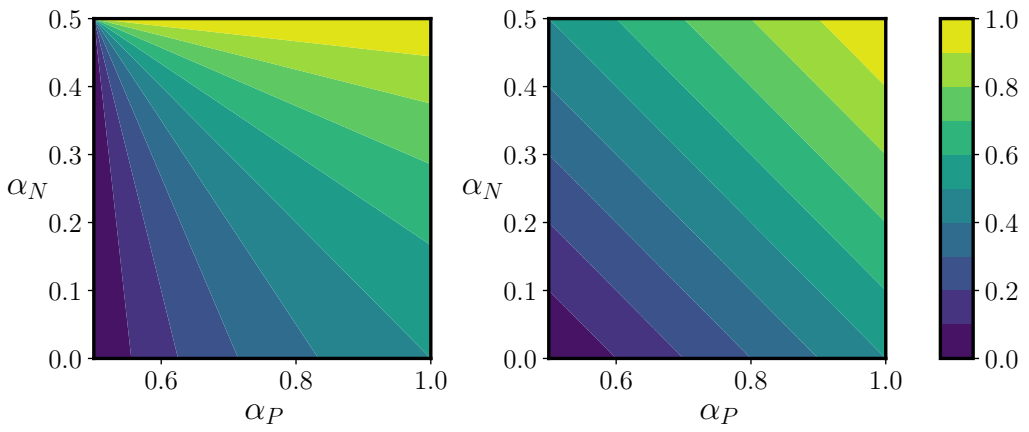

Figure 3: Contour plot of λ computed from Eq. 5 (left) and from Eq. 6 (right) for wet cell P and dry cell N.

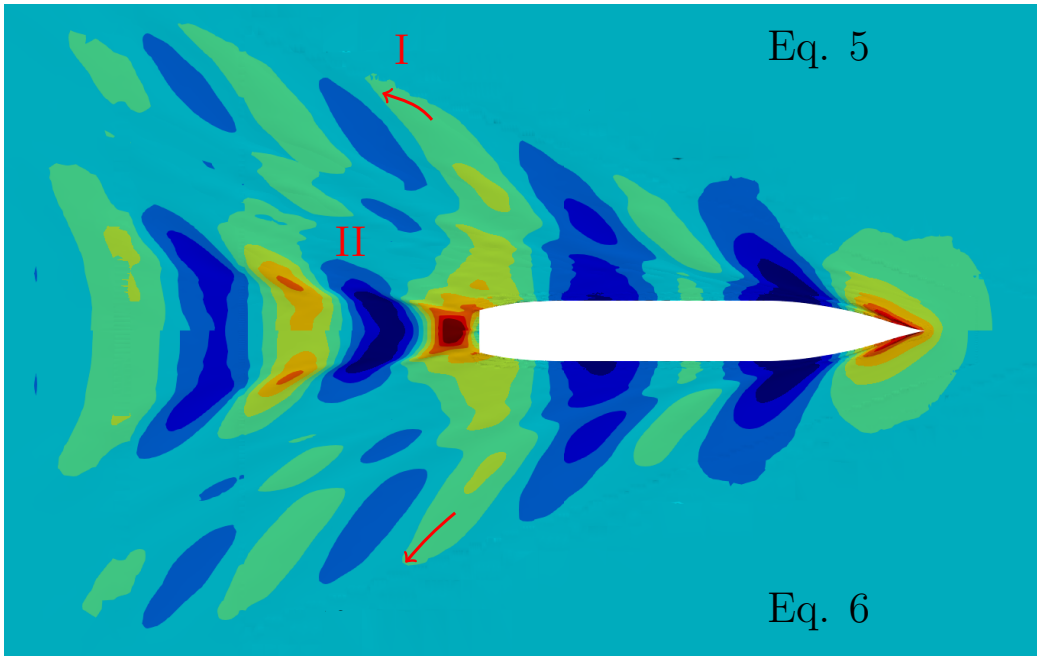

Figure 4: Kelvin wave in KCS case, top λ define by equation 5 and below λ defined by 6. I Difference of a wave tip bent, II disturbances on the wave shape. Here, Eq. 6 is utilized.

2.2.3. Discretization schemes

All RANS simulation presents steady-state simulation which is reached by using the local time stepping (LTS) scheme, named by localEuler in OpenFOAM. The method is the first order accurate with spatial varying time step. Other numerical schemes are shown in Table 4

Table 4: Numerical schemes in RANS cases.

term	scheme
gradient ∇	Gauss linear
gradient $\nabla(\vec{u})$	cellLimited Gauss linear
divergence $\nabla \cdot (\phi\ \vec{u})$	Gauss vanAlbada
divergence $\nabla \cdot (\phi\ \alpha)$	Gauss vanLeer
divergence $\nabla \cdot (\phi\ k)$	Gauss upwind
divergence $\nabla \cdot (\phi\ \omega)$	Gauss upwind
Laplacian ∇^2	Gauss linear uncorrected
cell to face interpolations	linear
component of gradient normal to a cell face	limited 0.333
divergence $\nabla \cdot (\phi\ \vec{u})$	Gauss linear upwind (DES-RANS region)
divergence $\nabla \cdot (\phi\ \vec{u})$	Gauss linear (DES-LES region)

2.3. Propulsion model

In this study KP505 propeller is modelled with an actuator disk source term which includes axial momentum and swirling source. Implementation of the actuator disk source is based on the method proposed by Hough et al. [31] where the radial distributed source term is shown. More details about how the radial distribution including propeller hub diameter is derived is shown in [32].

The Propeller thrust and torque is defined based on coefficients K_T and K_Q values from the experimental open water data. The model test is carried out with scale 1:31.6, a graph of the data is shown in Figure 5. Advanced coefficient J is calculated with given reference velocity U_{ref} and rotation speed n [1/s]

$$J = \frac{U_{ref}}{nD} \tag{7}$$

where D is the propeller diameter. In this study the reference velocity U_{ref} is defined by the volume average of an axial component of the actuator disk cell zone in the towing simulation. Details about the actuator disk model is shown in Appendix A.

2.4. Surface roughness

2.4.1. Roughness definitions in the literature

Average Hull Roughness (AHR) is the commonly used unit for hull roughness. AHR is defined in meters as an average of several measured samples of

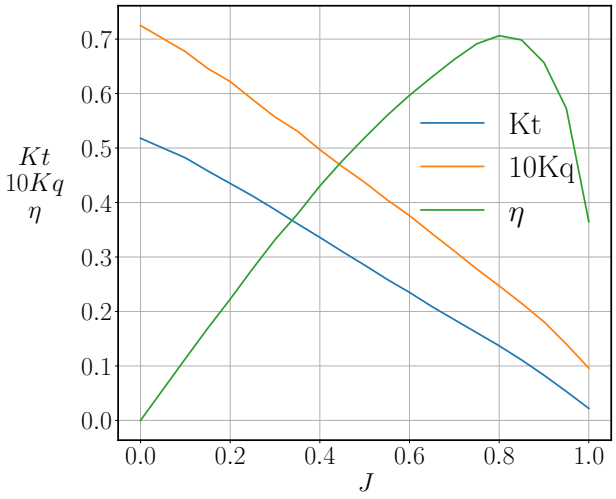

Figure 5: KP505 open water model test characteristics [24].

the maximum peak to through roughness height R_t over 50 mm length. Also the notation Rt_{50} is often used in the literature. The representative range of the coating and fouling roughens is from 30 to 10 000 μm with k_s. Schultz propose $k_s = Rt_{50}$ when $k_s > 1000$ [33]

In their study, Schultz [34] compare silicone and other paint coatings in flat plate experiments with unfouled, fouled and cleaned conditions. The roughness range, by using center line average roughness R_a, ranges from 12 to 20 μm for newly painted surface and 10 to 22 μm for a cleaned surface. In terms of R_t, these intervals correspond to 66 to 129 and 76 to 135 μm respectively. The roughness in all conditions is defined by the roughness function ΔU^+ and k^+ values. Such values are possible to define using the measured flat plate friction and dimensions, for example, using the Granville [35] method as is done in Schultz's study. Cases in clean and fouled condition results fit well to the Grigson roughness function $\Delta U^+ = \frac{1}{\kappa} \ln(1 + k^+)$ [36]. The same function is plotted in Figure B.20 in Appendix B. Schultz proposes correlations for roughness scale $k = 0.17R_a$ and in the fouled case $k = 0.059R_t\sqrt{SC}$ where R_t corresponds to the highest barnacles and SC to the percentual surface coverage. In this experiment unfouled condition ΔU^+ reaches level 1 respectively $k^+ < 0.6$ and in fouled condition ΔU^+ reach level 17 and k^+ is up to 1000.

A comprehensive experiment on marine coating roughness effects was car-

ried out by Yeginbayeva et al. [37]. In this case the measured roughness R_a is in the range of 2.0 to 28.82 μm and the experimental data fits again well to the Grigson roughness function. The roughness function ΔU^+ values stay below 4.5 and k^+ below 4 respectively. Based on this data $k = 0.14R_t$ i.e. $k = 0.6R_a$ are being presented as being inconsistent with the previously mentioned values. As an explanation, Yeginbayeva et al. [37] propose a roughness filtering in the measured data.

The flat plate experimental data of the barnacle fouled conditions has been presented in [38, 39]. The test matrix consists of three sets of barnacle height h, from 1.25 mm to 10 mm and four coverage SC levels 10 % to 50 %. The new roughness scale function [38] $k_G = f(SC, h)$ is presented which fits better to the Grigson roughness function as Schultz's equivalent. For example, choosing barnacle heights h 5 and 10 mm and SC 10 % leads to a roughness scale $k_G = 174$ μm by increasing SC upto 20 % $k_G = 445$ μm. Respectively h 1.25 mm and SC 10 % $k_G = 24$ μm and SC 20 % $k_G = 63$ μm.

2.4.2. Boundary layer similarity

It is already noted that the boundary layer thickness depends on the hull roughness. Validation data on how well RANS simulation can predict the roughness effect to the boundary layer thickness is scarcely available. Previous numbers give an idea of the range surface roughness ratio to the boundary layer thickness. With the ship Reynolds number and Prandtl power-law it is possible to estimate boundary layer thickness δ in the aft body. With $Re_x = 2 \times 10^9$ at location $x = 200$ m gives $\delta \approx 1$ m. In the heavy fouling case the thickness ratio $\delta/k_s \sim 100$. The velocity profile similarity is shown to be valid if $\delta/k_s > 40$ at the height Reynolds number [40–42]. Also outer-layer similarity states that turbulence motions are independent of wall roughness [43].

At the high Reynolds number $Re_\tau \approx 70000$ logarithmic mean velocity profile reaches $y^+ \approx 10000$ by $U^+ \approx 30$ [44] for smooth flat plate. Similar Reynolds number dependency is shown in [45] for a rough flat plate. We can conclude that a heavy fouled hull roughness is in range of the velocity profile similarity. This finding is not enough to estimate roughness effect to the boundary layer thickness.

2.4.3. Roughness model theory

In general, the boundary layer is presented by the logarithmic law by value of the dimensionless velocity $U^+ = \frac{U}{U_\tau}$ which is a function of the viscous term

$y^+ = \frac{yU_\tau}{\nu}$ where there is a scaling parameter friction velocity $U_\tau = \sqrt{\frac{\tau_w}{\rho}}$, kinematic viscosity ν and a wall distance y. The boundary layer flow depends on the wall roughness and one important phenomenon is the fully rough flow condition (FRFC) presented by Nikuradse [46]. In this condition the logarithmic law depends only on roughness k and the viscous term vanishes. The experiments carried out with the rough pipes and additional term $\Delta U^+(k^+)$ to logarithmic law is presented here. The same term is assumed to be valid also for the flat plate.

$$U^+ = \frac{1}{\kappa} \ln y^+ + B - \Delta U^+(k^+) \tag{8}$$

Where $k^+ = \frac{U_\tau k}{\nu}$ is the roughness Reynolds number, κ is the von Kármán constant 0.41 and constant $B = 5.1$. In the FRFC an offset constant in the logarithmic law is 8.48 [46] or 8.5 [22, 45] and then the log-law is reduced to form.

$$U^+ = \frac{1}{\kappa} \ln k_s^+ + 8.5 \tag{9}$$

In the FRFC the flat plate skin-friction coefficient and boundary layer thickness is independent of the Reynolds number [47]. There is no exact limit for FRFC and it depends on the used roughness scale k. With Prandtl-Schlichting the sand grain roughness regime is $k^+ > 60$ [22] or the equivalent sand grain roughness $k_s^+ > 70$ [45, 47].

In the present study the boundary layer is modelled with the wall function. Both smooth and rough walls are simulated by using velocity based wall functions *nutUWallFunction* and modified *nutURoughWallFunction*. The original *nutURoughWallFunction* wall function includes the roughness function which overlaps by the Grigson function at FRFC by the roughness parameter $C = 1$. The original OpenFOAM wall function is validated by a wind tunnel experiment [45] to ensure the RANS model capability predicts the boundary layer thickness. In this case P36 grit sandpaper is used which presents the evenly distributed roughness and FRFC is also realized. The details and validation of the rough wall function *nutURoughWallFunction* is shown in Appendix B and Appendix C. For ship simulation purpose the wall function is modified so that the Grigson roughness function with all k^+ values is used.

2.4.4. Choice of the roughness values for the KCS

The surface roughness in this study means the hull roughness caused by paint, antifouling coating or biofouling. A conclusion of the relevant ship hull roughness level in fouled condition is that it can be one magnitude higher than in an unfouled condition. The aim in this study is to find a realistic hull roughness combination in order to define the boundary layer thickness variation in the aft body.

The selected roughness values in the present study correspond to the values in the previous literature [34, 38, 48]. To make results comparable the used roughness function must also must be the same. Relevant references are: The Demirel et al. [38] experiment where the data is fitted to the Grigson roughness function and Song et al. [49] study where a KCS hull simulation is carried out with the Grigson roughness function. Due to the interest also the low and moderate roughness effect is necessary to capture the transition rough condition (roughness scale $k_G < 20\mu$m). Based on a review of literature, the Grigson roughness function is also valid for this region.

The selected roughness values are, for new antifouling 2.59 μm [48], slight fouling $k_G = 24$ μm and moderate fouling $k_G = 489$ μm [38]. The roughest case presents a heavy fouled antifouling based on Schultz [34] experiment, where is 7 mm height barnacles by 75 % coverage gives $k_G = 0.059 \times 7 \times \sqrt{75}$ = 3580 (μm).

2.5. Analysis of resistance distribution

In the present work, resistance components are shown by the distribution along the hull surface to make it possible to separate areas where the hull roughness, propulsion or numerical method causes a deviation. For example, all resistance coefficients $C = \frac{2F}{\rho S U^2}$ are shown in Figure 6 where they are divided to 50 parts in the longitudinal direction. Top left in the Figure 6 presents the pressure resistance coefficient C_P distribution by using the total pressure $p = p_d + \rho\vec{g} \cdot \vec{x}$ where p_d is the dynamic pressure and hydrostatic part $\rho\vec{g} \cdot \vec{x}$. It must be stated that the hydrostatic part dominates in the presented distribution and it can be seen by comparing the same case (S) results in Figure 1 where dynamic pressure p_d is used. The propulsion effect to the resistance distribution can be seen at the right side in the Figure 6 where the difference of local resistance coefficient between the cases is shown. Highest difference between cases is in the aft, as is expected. The negative difference means more resistance and vice versa i.e. difference means the reference case (S) minus case where it is compared (SP).

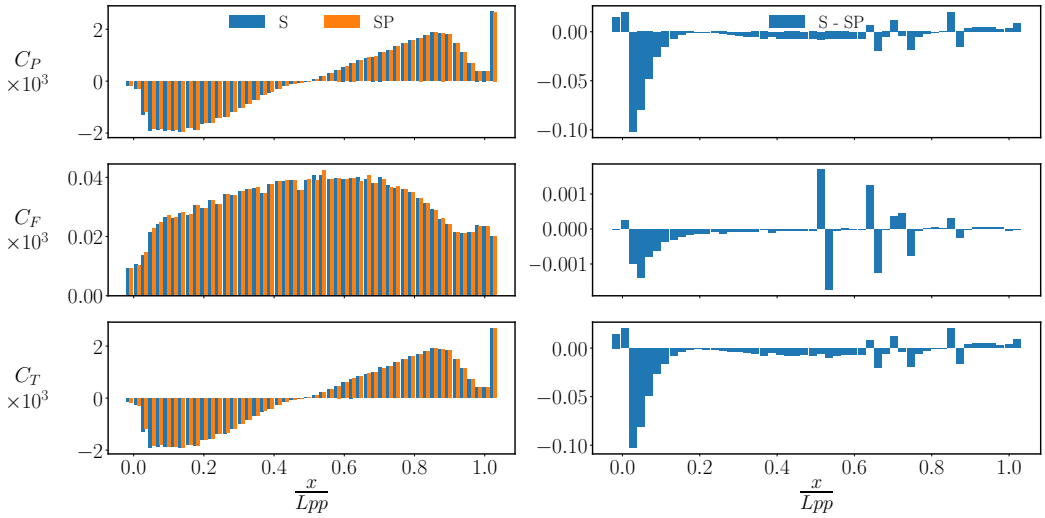

Figure 6: At left smooth case S resistance components distribution on the hull surface in towed and propulsion (P) condition. At right difference of smooth case towed and propulsion condition. At the top row, pressure middle friction and down total resistance coefficient

In this method, the surface area of the parts is not precisely the same and it causes differences to neighbouring parts in the coefficient distributions. This becomes more visible by increasing the parts number as in submodel approach as is presented later. In this work all the results of the resistance forces or coefficients are defined by the total pressure $p = p_d + \rho\vec{g} \cdot \vec{x}$.

2.6. The submodel approach

2.6.1. Submodel setup

As mentioned earlier, an attempt is made to validate the RANS results using a submodel approach in the stern part, where the wave breaking effects are pronounced. A schematic of the submodel approach is presented in Figure 7. The simulation steps of the submodel approach are organized so that at first a preliminary RANS simulation is carried out for the whole ship. Secondly, the hull position and orientation is taken from the preliminary simulation and the submodel mesh is constructed for the stern part. Thirdly, a cutplane consisting the velocity field as well as the volume fraction field is taken from the preliminary simulation. The data in the cutplane is used as an (inlet) boundary condition in the submodel. Since the data obtained from the preliminary simulation is the steady-state (Reynolds averaged) solution

a numerical tripwire [50] is used in the submodel to trigger the transient effects.

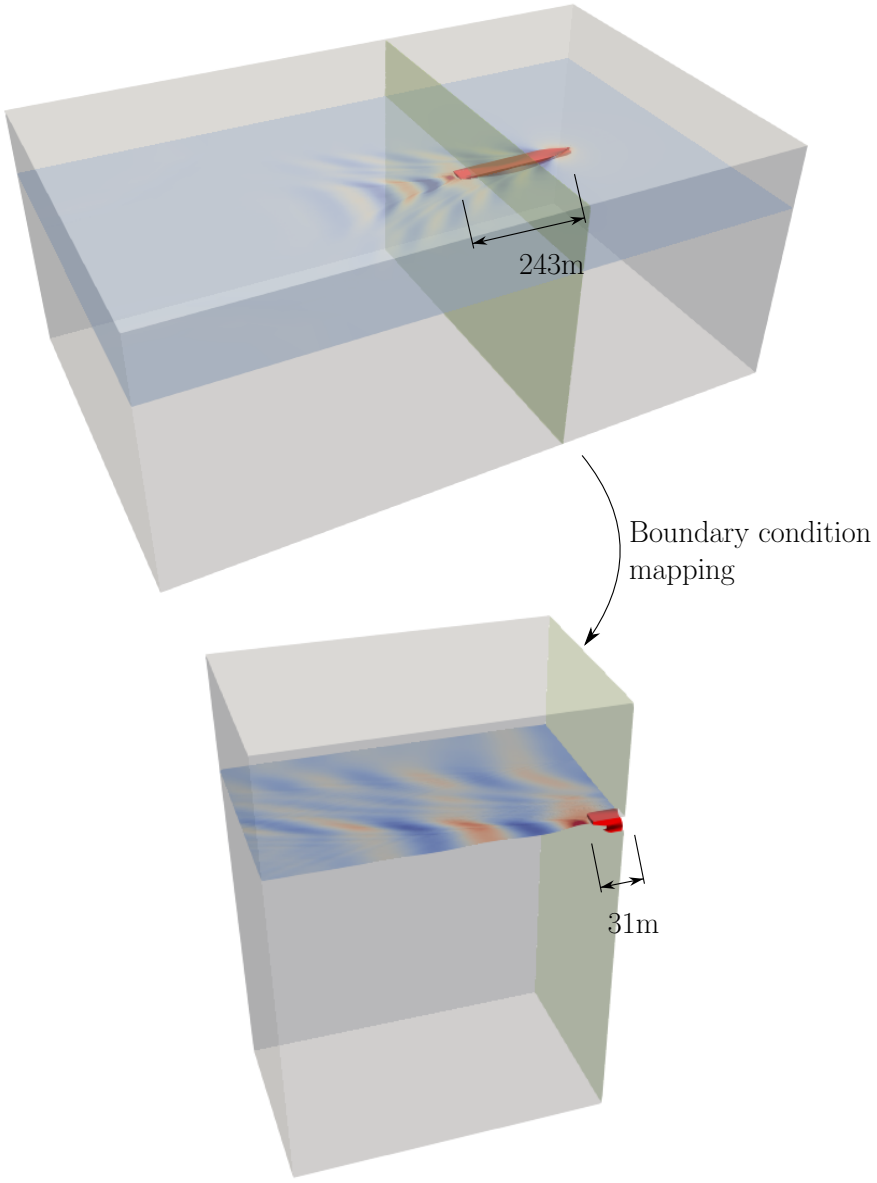

Figure 7: A schematic of the submodel approach. The full-scale preliminary RANS simulation is shown in the top figure and the submodel stern simulation in the bottom figure.

2.6.2. Submodel validation

To validate the mapping of the boundary condition we carry out a RANS simulation both for the full and submodel with exactly same numerics and grid resolution. To compare the results the resistance coefficient is investigated by dividing main and sub model to equal length pieces. In case main model total length 243 m and sub model 31 m common divisor is 1 m. By subtracting a resistance force piece by piece it is possible to gain an error which is caused by the sub model method. In the test case it is calculated a steady RANS case by using the same mesh resolution in the both models. The comparison is shown in Figure 8.

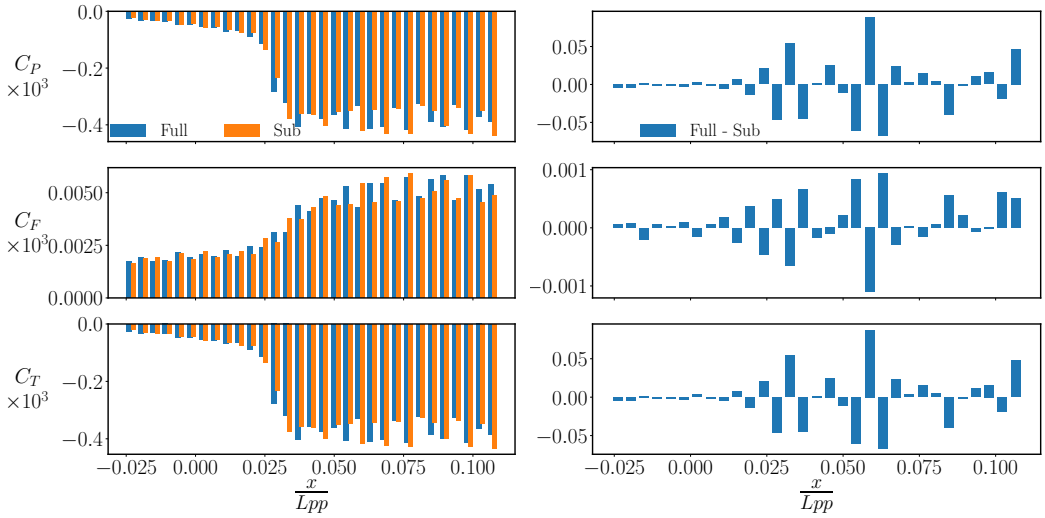

Figure 8: At left case S main and sub model resistance components distribution on the hull surface. At right difference of main and sub model. At top row pressure, middle friction and down total resistance coefficient

The deviation between the main and sub model is calculated by the sum of the coefficient's difference. Deviation is compared to main model coefficients, it is for pressure 0.85 %, friction 0.14 % and total 0.19 %. Methods seem to give an even resistance distribution in range $\frac{x}{Lpp} < 0.02$ from transom towards the bow. Towards the front, the propulsion may cause more deviation which is visible in 0.02 to 0.07 $\frac{x}{Lpp}$ range, see Figure 8.

3. Results

3.1. RANS and surface roughness effect

It is well acknowledged that the surface roughness affects primarily the friction resistance while its impact on the pressure resistance remains secondary. In the present work, it will be seen that surface roughness links closely to the pressure distribution in the aft body. Such a connection can also be seen in the pressure coefficient distribution difference between the smooth and the roughest case on the right hand side of Figure 9 where the difference is small when the horizontal coordinate $\frac{x}{Lpp} > 0.3$ except in the bow. In the aft body pressure resistance decrease is in the range $0.1 < \frac{x}{Lpp} < 0.3$ and increases when $\frac{x}{Lpp} < 0.1$. The difference in C_P distribution in the aft body looks similar as the pressure resistance which is calculated based on the dynamic pressure p_d in Figure 1. In the roughest case the acceleration of the velocity must be lower in range $0.1 < \frac{x}{Lpp} < 0.3$ causing less resistance and due to the lower velocity level the speed decrease does not cause as high dynamic pressure to the rest of the hull length $\frac{x}{Lpp} < 0.1$. In summary, a higher pressure resistance for the roughest case results. A summary of the RANS results in towed/propulsion cases is shown in Table 5 / 6.

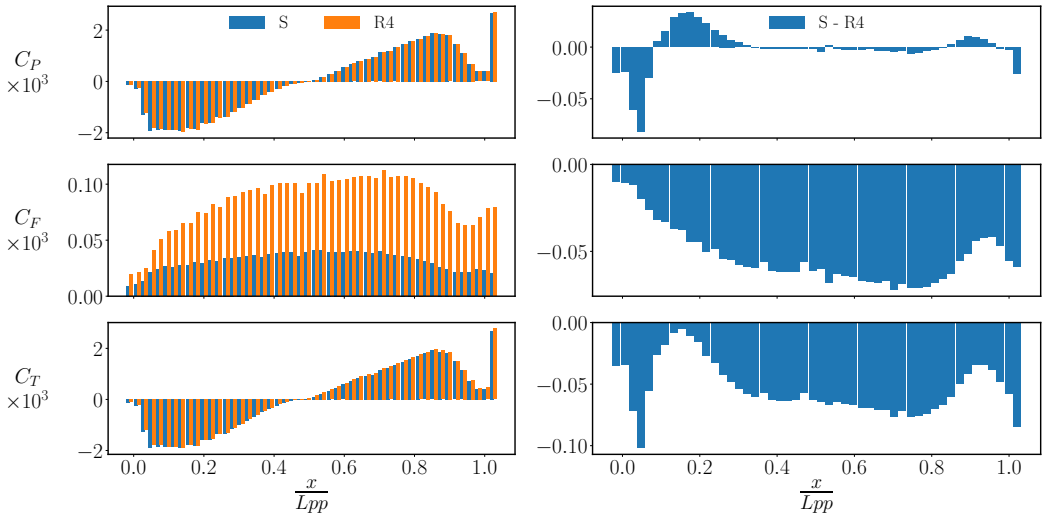

Figure 9: At left resistance components distribution in smooth and rough R4 case and at right difference of cases.

The effect of the hull roughness on the stern the wave shape and velocity field in the aft is shown in Figure 10. The velocity profile is taken from

the stern corner downwards below the baseline. Increasing hull roughness decreases the height of the wave crest and it moves towards the transom. Respectively, the roughness increases the boundary layer thickness and it is visible in the velocity profiles. In the propeller wake velocity profiles are closer to one another independent of the roughness. The surface roughness affects flow separation from the transom. In the two roughest R3 and R4 propulsion cases the transom stays wet. Respectively, in cases S, R1 and R2 the stern wave remains higher in the propulsion case. In fact, the effect of the boundary layer thickness on the stern wave profile was recently investigated by the authors [8] for a simple immersed flat plate. The present observations on surface roughness are consistent with the previous study: a thicker boundary layer decreases the first stern wave height due to the slower fluid flow before the transom. In the ship operation perspective the hull roughness is considerable design parameter. The moderate fouling effect to the boundary layer thickness is comparable to the simulation in the model-scale.

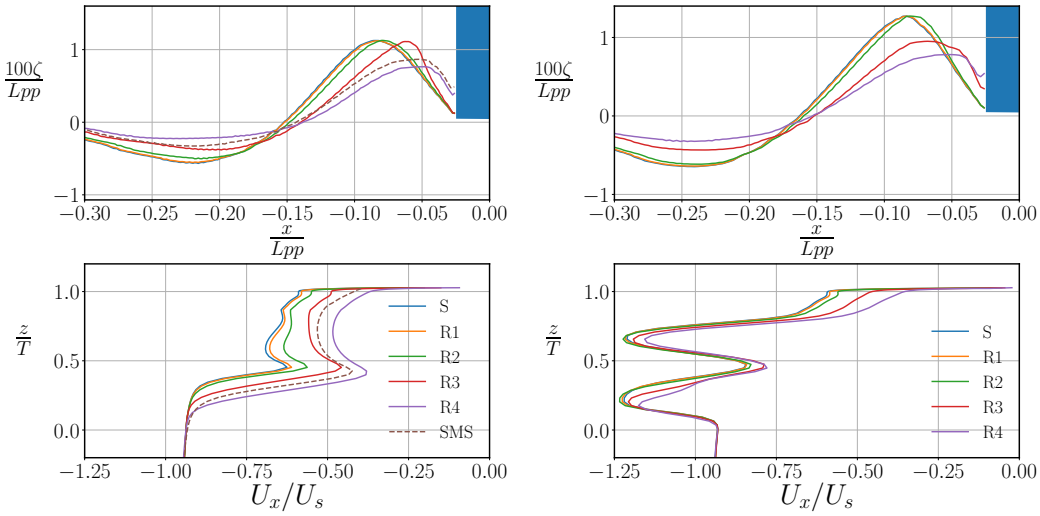

Figure 10: Top stern wave elevation ζ and bottom velocity profile from the transom corner to downward with smooth and four hull roughness. At left towed and at right with propulsion. Blue box represents ship transom. SMS is model-scale 31.6 case.

Boundary layer thickness is visualized also in Figure 11 where it is shown in the smooth and the roughest case. It is essential to note that in practice the boundary layer thickness is not only affected by $\frac{x}{Lpp}$, but also by the adverse pressure gradient due the hull shape. Reduction of the stern wave

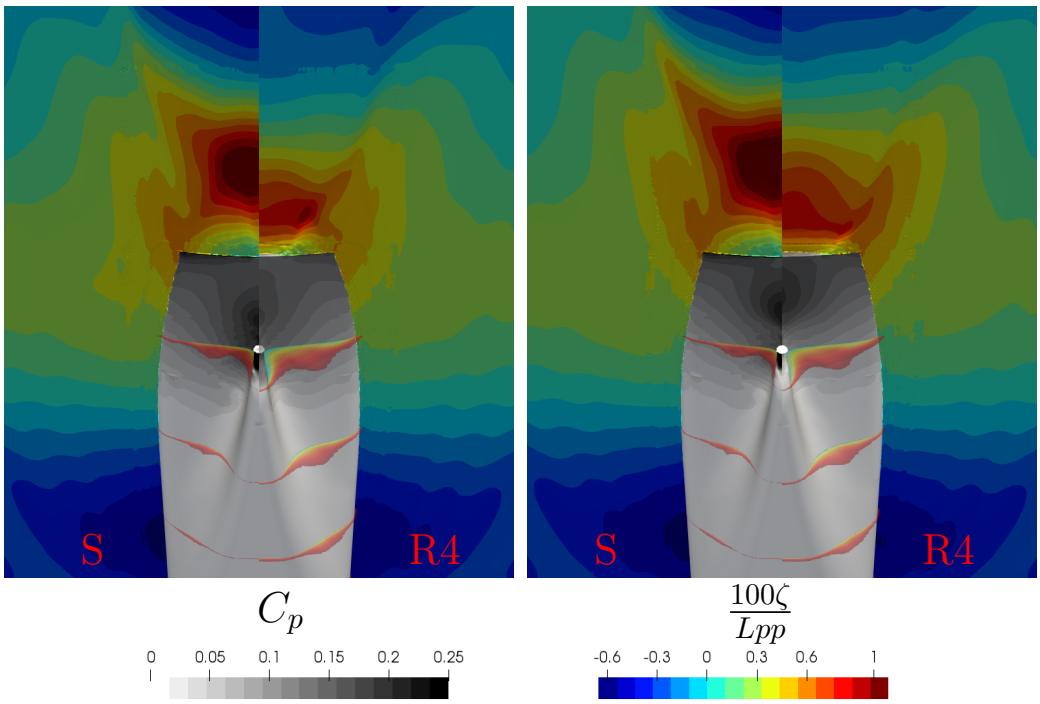

Figure 11: Aft body viewed from the bottom side where at the left is a towed, and at right, a propulsion case. In the hull surface the pressure coefficient C_p calculated from dynamic pressure p_d and wave elevation ζ. Boundary layer thickness is presented with cut planes by colored range $0 < \frac{U_x}{U_s} < 0.9$.

height is also clearly visible and in the rough cases the propulsion caused a larger wetted area in the transom. Pressure and velocity fields in the aft body are similar as is presented [49].

Next, the resistance coefficient in the towed case is compared to the literature and presented in Figure 12. We note that pressure resistance C_P in the CFD results is comparable to the residual resistance in the ship resistance scaling term. The results indicate an increasing pressure resistance trend due to the increasing hull roughness. We note that the reference data [13, 49] represents a different simulation setup for the KCS hull than in the present work. In the present study a rudder is not included and the simulation is carried out with free sink and trim in contrast to references [13, 51] and [49] where fixed hull with a rudder is used. The smooth case friction resistance is higher than in the references. One reason is a free sink which causes a

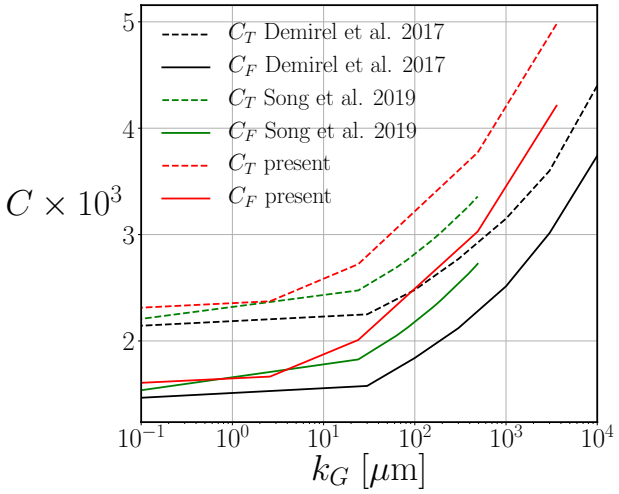

Figure 12: Resistance components comparison to literature in the towed case by the hull roughness function, Demirel [13] Song [49].

higher wetted surface area being about 5 % higher in the present simulations than the reference area S. The observed friction resistance change ΔC_F is well in line with Song et al. [49] where the Grigson roughness function was also used with the SST $k-\omega$ turbulence model. The convergence study is shown in Appendix D for the pressure resistance, stern wave shape and the velocity profile. The convergence is not very sensitive to the chosen tolerance level. We can conclude that in the present results the iterative uncertainty in pressure resistance is less than 10 %. Respectively the stern wave shape and velocity profile are not sensitive to the chosen tolerance level.

Table 5: Towed cases results. Sinkage s and trim angle θ positive direction pow down. Friction resistance coefficient change ΔC_F is compared to smooth case.

	k_G [μm]	C_P $\times 10^3$	$C_F\times$ $\times 10^3$	C_T $\times 10^3$	s [m]	θ [deg]	ΔC_F [%]	k^+_{avg}
Ref. [51]	32	0.850	1.570	2.334				
Ref. [13]	0	0.676	1.421	2.097				
Ref. [49]	0	0.679	1.446	2.095				
Ref. [49]	24	0.649	1.826	2.475			29	
Ref. [49]	489	0.634	2.725	3.358			93	
Ref. [14]	489							195.8
S	0	0.706	1.565	2.270	0.547	0.169		
R1	2.59	0.708	1.665	2.373	0.547	0.169	6.4	0.75
R2	24	0.713	2.009	2.722	0.546	0.168	28	7.64
R3	489	0.743	3.028	3.772	0.544	0.166	94	191.9
R4	3580	0.767	4.211	4.979	0.542	0.166	169	1663.2

The effect of the hull roughness on the propulsion coefficients ($1-w$ and $1-t$) is summarized in Table 6. In the present study, the hull roughness increases the boundary layer thickness which decreases the wake factor $1-w$ significantly. A similar trend has been previously observed in the literature [15, 49]. Increasing surface roughness results as a subtle rising trend in the trust deduction coefficient $1-t$. Here, $1-t$ is calculated from the total resistance ratio between the towed and propulsion cases i.e. propeller thrust is assumed to be exactly the same as the resistance. The actual propeller thrust is not used due to the propulsion operation point being iterated manually, the actual difference between thrust and resistance is less than 1 %. However, authors [15] report numerical uncertainty for the coefficient $1-t$ which may explain the discrepancy. The advance coefficient J decreases due to the increasing hull roughness and the trend is in line with the reference value reported previously in the literature [15].

Table 6: Propulsion cases results.

	k_G [μm]	C_P $\times 10^3$	C_F $\times 10^3$	C_T $\times 10^3$	$1-w$	$1-t$	J
Ref. [51]	32	1.145	1.577	2.773	0.812	0.842	0.714
Ref. [15]	0				0.773	0.867	0.729
Ref. [15]	413				0.714	0.856	0.609[1]
Ref. [15]	2065				0.682	0.852	0.545[1]
Ref. [49]	24				0.765		
Ref. [49]	489				0.712		
S	0	1.068	1.570	2.638	0.829	0.861	0.737
R1	2.59	1.082	1.671	2.753	0.825	0.862	0.727
R2	24	1.112	2.018	3.130	0.808	0.870	0.698
R3	489	1.141	3.042	4.183	0.745	0.902	0.616
R4	3580	1.185	4.234	5.420	0.658	0.919	0.525

[1] Propeller open water data includes surface roughness effect.

The roughness Reynolds number in case R4 is shown in Figure 13, also average k^+ values is shown in Table 5.

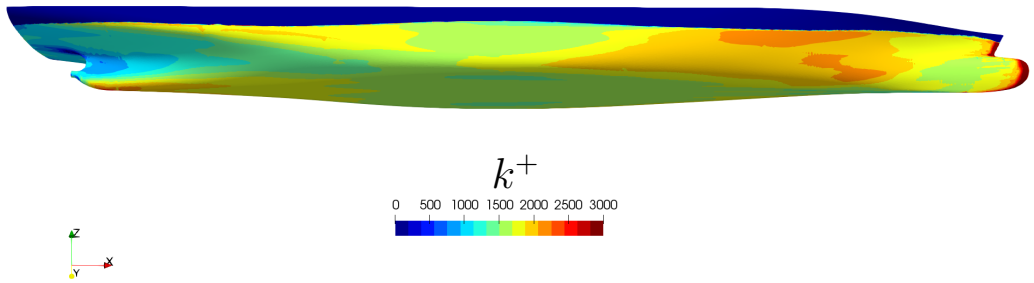

Figure 13: k^+ distribution in the hull surface, case R4.

3.2. DES

Altogether three DES submodel simulations were carried out. The simulated models were the smooth model (S-DES) with and without propulsion as well as the roughness level R4-DES without propulsion. Figure 14 shows an illustration of the instantaneous free surface and the velocity field taken from the middle of the ship. As can be qualitatively seen from the figure, the scale-resolving simulations indicate a highly turbulent wake dynamics.

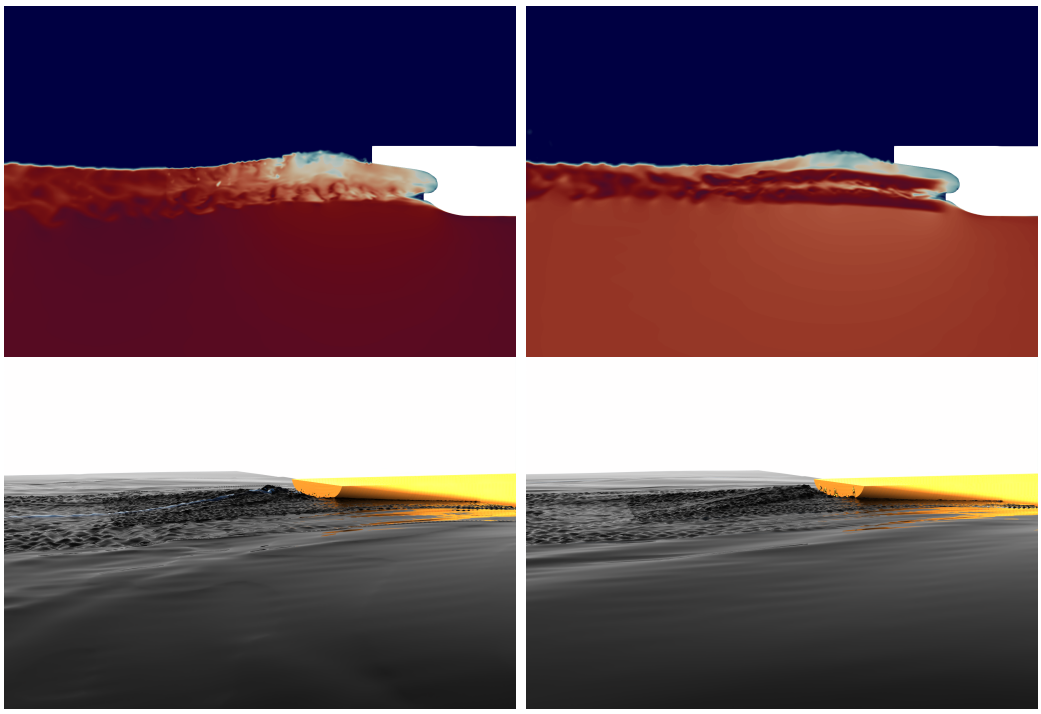

Figure 14: Instantaneous snapshot of the velocity field taken from the middle of the ship and the free surface. The results are taken from the S-DES simulation without propulsion (left) and with propulsion (right).

Figure 15 shows the mean free surface elevation at the middle of the ship as well as the streamwise velocity profile taken at the transom corner. Both the DES submodel simulations and the corresponding RANS simulation are shown in the figure. For the smooth simulation (S) without propulsion, S-DES indicates a mildly wetted transom while the RANS simulation shows a dry transom. When the propulsion effects are included in the smooth hull simulations, both RANS and DES indicate a dry transom. However, in the S-DES simulation the shape of the first wave crest is quite different than what the RANS indicates. The shape of the DES wave crest is more sharp and bends slightly towards the transom indicating wave breaking [8]. In the rough hull simulations both R4 and R4-DES indicate a wet transom. The mechanism leading to the transom wetting in R4 and R4-DES is the loss of momentum in the boundary layer which can be seen from the velocity profiles. The wave pattern in the DES simulations is further illustrated in Figure 16.

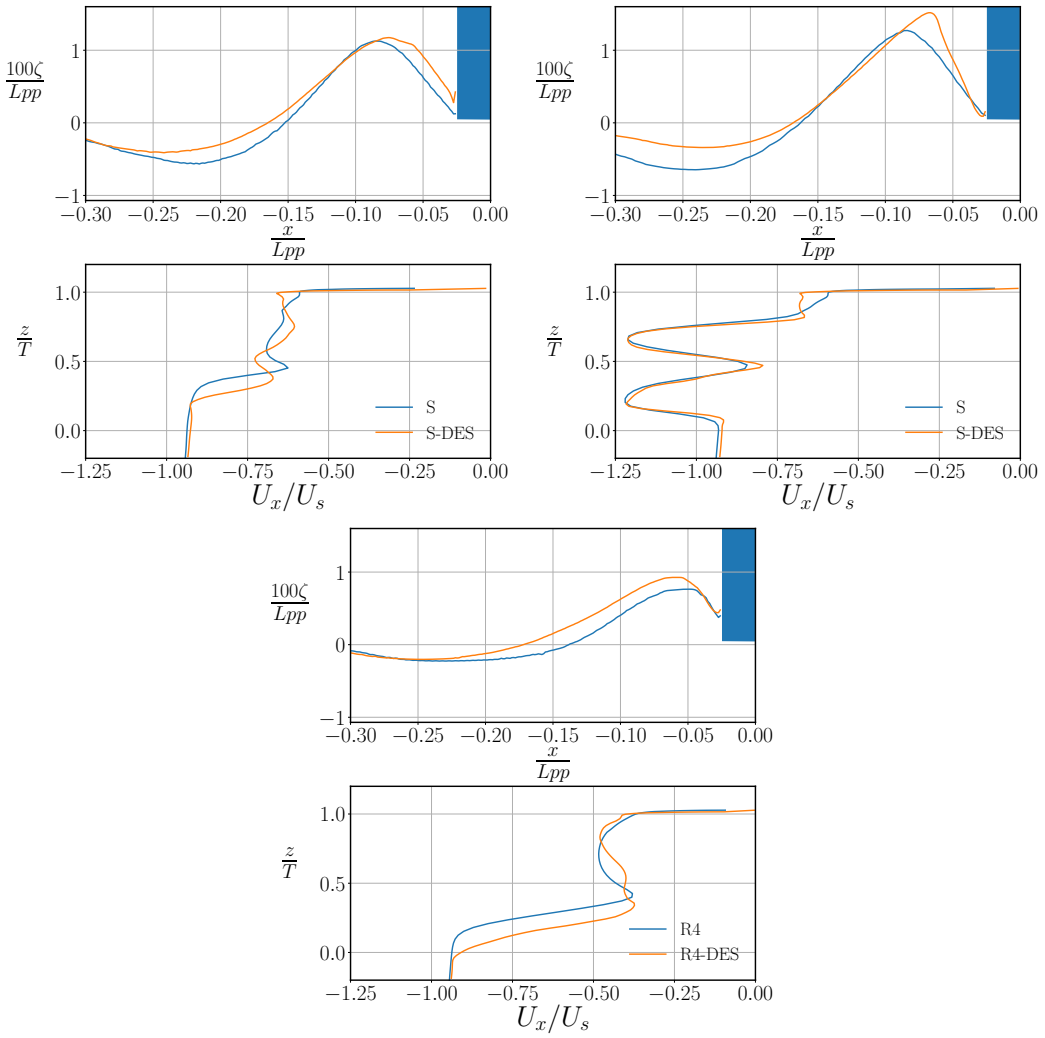

Figure 15: At top stern wave elevation ζ and bottom velocity profile from the transom corner to downward with smooth and four hull roughness. At left towed and at right with propulsion. Blue box represents ship transom.

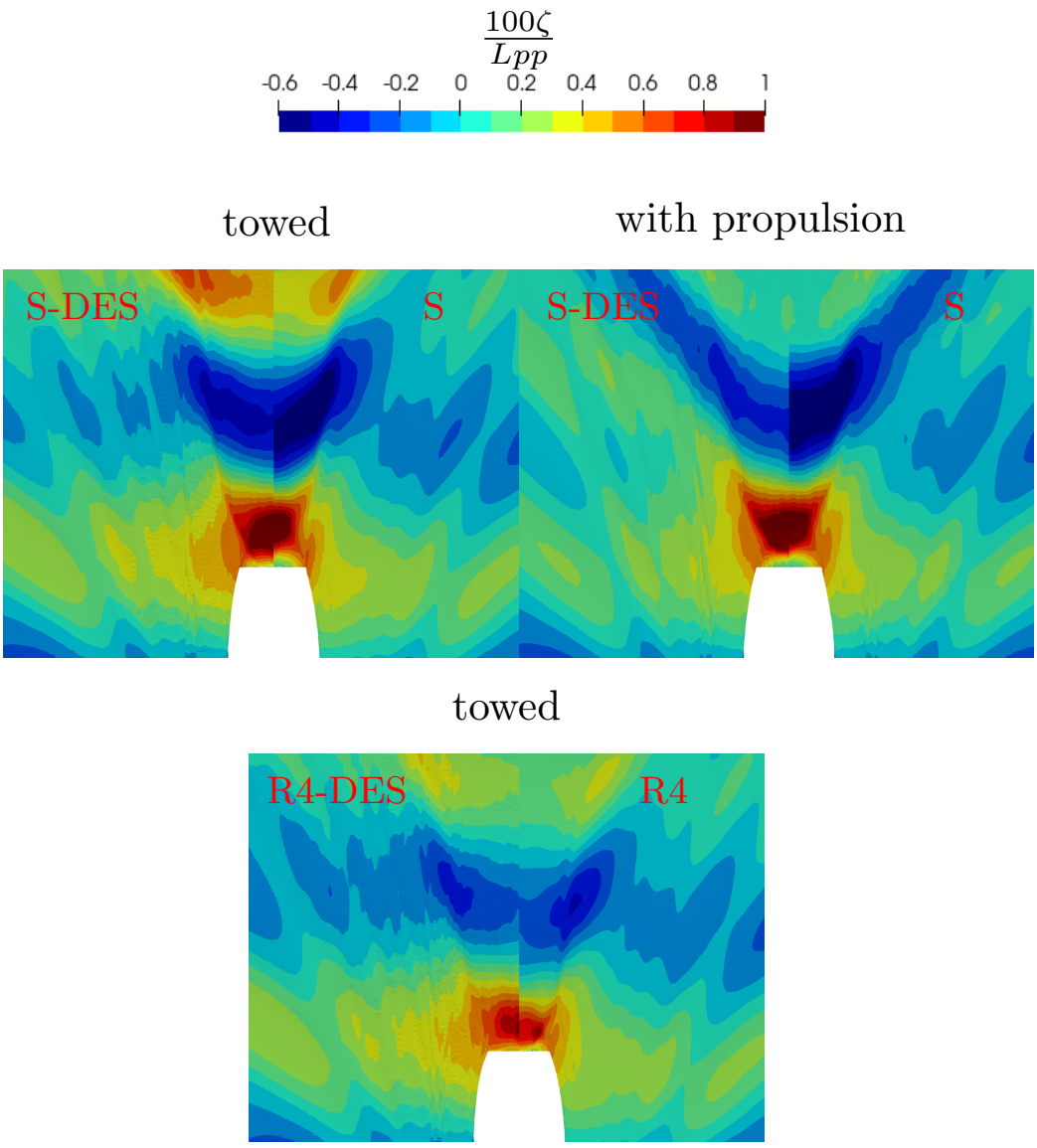

Figure 16: The wave elevation ζ from the DES simulations compared to the corresponding RANS simulation.

Figure 17 shows the pressure and viscous resistance components from the DES simulations and the corresponding RANS simulations. The DES results indicate consistently lower viscous resistance than the RANS counterparts. Such a trend is likely caused by the different near-wall turbulence model.

In the DES, the S-A model is used in the near wall cells while the RANS simulations were carried out with the SST $k-\omega$ model.

It is clear that the S-A model underpredicts the surface roughness effect. Roughness corrections to the S-A model, as proposed by Spalart and Aupoix [52, 53], are not implemented to the OpenFOAM S-A model. The roughness treatment requires non-zero value of $\tilde{\nu}$ on the wall. In the present study $\tilde{\nu}$ is 0 on the wall in all simulations. The same velocity based ν_t wall function in both turbulence models is used where the Grigson roughness function offset term is added. We note that the used wall roughness implementation is not exactly in line with the original implementation by Spalart and Aupoix. We note that the present near-wall implementation offers a good prediction in the stern wave despite the lower near-wall viscous resistance. We assume that the present approach does not change the conclusion about the wetted transom despite the fact that the additional resistance is not accounted for near the wall.

The S-DES results indicate a high pressure resistance component at the transom (at $x/Lpp \approx -0.025$) contrasting the RANS observations. The reason for the high pressure resistance in the smooth DES simulations in Figure 17 is likely to be the sharp reduction of velocity at the transom. In the towed case the velocity reduction is due to the transom wetting while in the propulsion case it is most likely due to the steep breaking wave profile. The rapid reduction of velocity is seen as an increased pressure loss. In the R4 case no increase of pressure resistance is observed at the transom in Figure 17 although the transom is fully wet. In the R4 case, the pressure loss occurs already in the thicker boundary layer before the transom which can be seen from the significantly lower velocity values in Figure 15. Therefore, we conclude that transom wetting alone does not fully describe the increased pressure resistance. In fact, the sudden decrease of velocity (pressure loss) at the transom is linked to the increase of pressure resistance as seen from the velocity profiles in Figure 15. The difference in the pressure resistance at the transom between RANS and DES is tabulated in Table 7.

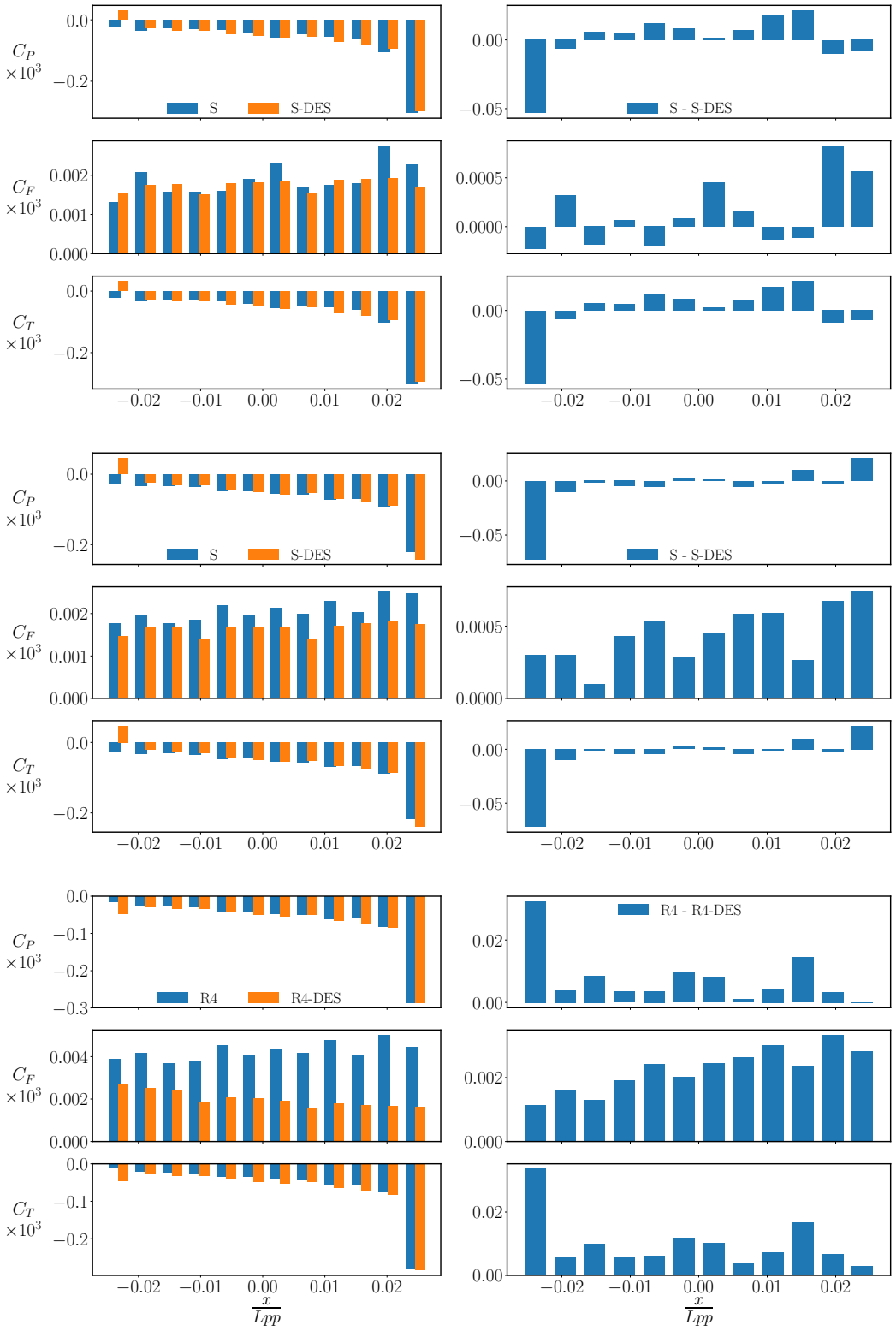

Figure 17: At left, the resistance coefficients from the DES simulations compared to the corresponding RANS simulations presented with one meter intervals. At right, DES results subtract from RANS results. From to bottom S towed, S propulsion and R4.

Table 7: The pressure resistance difference at last interval ($\Delta C_P = C_P^{RANS} - C_P^{DES}$) between RANS and DES methods and the ratio of the difference ($r_i = \Delta C_P / C_i^{RANS}$) to the whole hull's pressure C_P and total resistance C_T. Note that a positive difference indicates a higher resistance in DES.

case	$\Delta C_P \times 10^3$	$r_P[\%]$	$r_T[\%]$
S	0.053	7.5	2.3
S propulsion	0.073	6.8	2.8
R4	-0.032	-4.2	-0.7

The sudden reduction of velocity at the transom in S-DES results in high turbulence in the vicinity of the transom as illustrated in Figure 18. The figure shows the resolved, modelled and total turbulence kinetic energy from the DES simulations as compared to the respective RANS simulations. It should be noted that in the RANS simulations all the turbulence is modelled and only k total is shown. The S-DES simulations with and without propulsion indicate high (resolved) k value in the immediate vicinity of the transom while the R4-DES result indicates high k value downstream of the transom. The reason for the high k in the smooth simulations is the higher velocity in the hull boundary layer causing higher shear. A similar trend was observed earlier for a simplified transom configuration by the authors [8] when the boundary layer thickness was increased. It is interesting to also note the correlation between k and the wave shape between towed and propulsion S-DES cases. A high k value at the free surface can be considered as an indication of wave breaking [8]. For the propulsion case the high k spot occurs approximately at a location where the wave shape has high curvature. The high k spot, however, does not reach the transom for the S-DES with propulsion leaving the transom mostly dry.

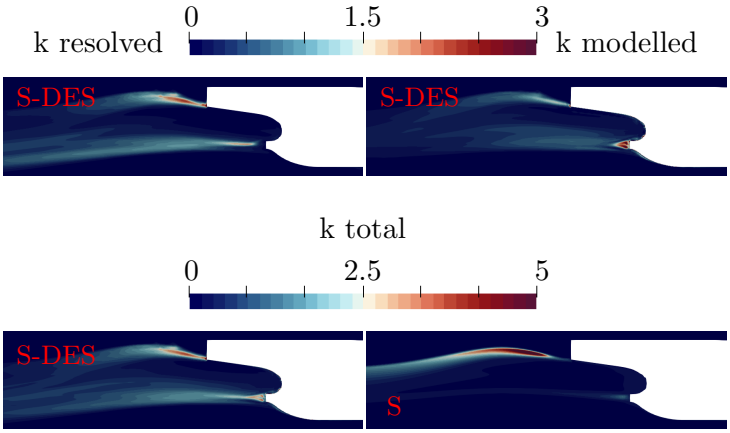

(a) DES and RANS result for a smooth hull without propulsion.

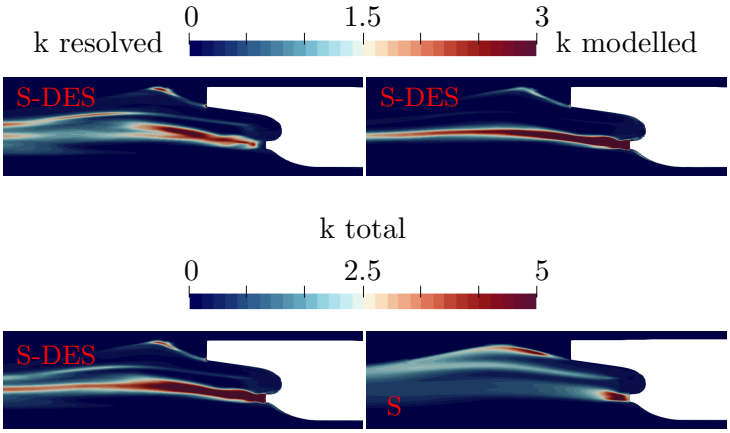

(b) DES and RANS result for a smooth hull with propulsion.

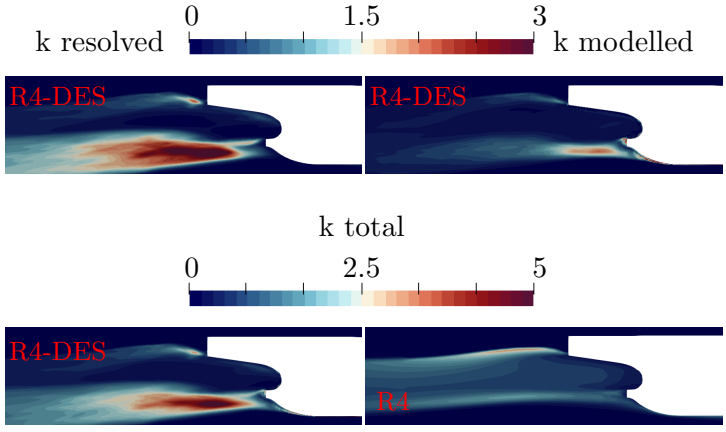

(c) DES and RANS result for the R4 surface roughness.

Figure 18: Resolved and modelled turbulence kinetic energy $k = (\overline{u_x u_x'} + \overline{u_y u_y'} + \overline{u_z u_z'})/2$ from the DES and RANS simulations.

4. Conclusions

Fluid flow phenomena in the ship aft body region were investigated with the KCS full-scale ship model in towed and propulsion cases at Froude number 0.26. Both, RANS modeling and scale-resolved turbulence modeling (DES) methods were utilized. DES simulations are carried out in a sub-model framework in the aft body only. Four different hull roughness values were used with a Grigson roughness function based wall model. The RANS model capability to predict boundary layer thickness is verified by the experimental flat plate data (see Appendix C). Different hull roughness values represent the new antifouling coating, slight, moderate and heavy fouling conditions. The effect of hull roughness, propulsion and turbulence model on the local resistance values were investigated.

As noted in the introduction, in various previous studies, the focus has been on the hull roughness effect to the viscous resistance. The present study clarifies the roughness definition and the modeling method. By using the same roughness length scale and roughness function in the wall model, it is possible to reproduce the same change to the viscous resistance as in the literature. Here, the same turbulence model is used as in the reference.

Quite often in the literature a hull roughness effect to the stern wave height is mentioned, but nearly in every case, a deeper analysis on the effect is lacking. In the present study is shown that the surface roughness increases the boundary layer thickness and reduces the stern wave height. The crest is also noted to move towards the transom with a thicker boundary layer. The thicker boundary layer i.e. lower flow velocity close to the hull has an affect to the pressure distribution, especially in the aft body, and that way it connects to the pressure resistance. The pressure resistance distribution is visible when $\frac{x}{Lpp} < 0.1$ where it increases and decreases when $0.1 < \frac{x}{Lpp} < 0.3$ towards the front of the hull where the effect remains minor. Naturally, a thicker boundary layer causes a major effect on the wake factor and the advance coefficient also changes the trust deduction coefficient.

In the moderate and heavily fouled conditions, thickness of the boundary layer is comparable to the model-scale equivalent and it also causes a wetted transom. From the energy efficient design point of view, the hull fouling makes one aspect to the scale effect discussion. The difference between the clean and fouled hull can be on the same level as the scaling effect i.e. difference of results between the model- and full-scale simulations. It is obvious that any ship will operate with the fouled hull during most of the time.

This work may be among the first DES studies on full-scale ships. Further differences between the DES and RANS can be summarized as follows. In the present DES cases, the transom remains wet due to the breaking stern wave. The differences between RANS and DES became more pronounced when propulsion was modeled. This can be explained by the higher level of turbulence in the stern wave which is resolved using DES. For this reason, the DES solution can be considered to be more accurate. For the smooth hull the DES results indicated 7.5% and 6.8% higher pressure (2.3% and 2.8% in total) resistance at the transom than RANS in the towed and propulsion cases, respectively. However, transom wetting alone does not fully describe the increase in pressure resistance. Both the DES and RANS with rough hull indicated lower pressure resistance at the transom than the smooth cases although the transom was observed to be fully wet. It seems that the velocity decrease at the transom correlate with the additional resistance component.

A major achievement of the study is to propose a simulation strategy for full-scale scale-resolved ship simulations via the DES submodel approach. The approach is shown to be feasible although still computationally heavy. To our knowledge, this work is among the first full-scale scale-resolved ship simulations.

Conflict of interest

None to declare.

Acknowledgement

The computational resources for this study were provided by CSC – Finnish IT Center for Science.

References

[1] Ittc – recommended procedures and guidelines. practical guidelines for ship cfd applications 7.5-03-02-03 (2014).
URL `https://ittc.info/media/4196/75-03-02-03.pdf`

[2] W. Sun, Q. Hu, S. Hu, J. Su, J. Xu, J. Wei, G. Huang, Numerical analysis of full-scale ship self-propulsion performance with direct comparison to statistical sea trail results, Journal of Marine Science and Engineering

8 (1) (2020) 24. doi:10.3390/jmse8010024.
URL https://doi.org/10.3390/jmse8010024

[3] L. Larsson, L. Zou, Evaluation of resistance, sinkage and trim, self propulsion and wave pattern predictions, in: Numerical Ship Hydrodynamics, Springer Netherlands, 2013, pp. 17–64. doi:10.1007/978-94-007-7189-5_2.
URL https://doi.org/10.1007/978-94-007-7189-5_2

[4] D. Ponkratov, Proceedings: 2016 workshop on ship scale hydrodynamic computer simulations, Lloyd's Register, Southampton, United Kingdom (2017).

[5] V. Bertram, Practical ship hydrodynamics, Elsevier Science, Burlington, 2011.

[6] E. Baba, A new component of viscous resistance of ships, Journal of the Society of Naval Architects of Japan 1969 (125) (1969) 23–34. doi:10.2534/jjasnaoe1968.1969.23.

[7] B. Starke, H. Raven, A. van der Ploeg, Computation of transom-stern flows using a steady free-surface fitting rans method, in: 9th International Conference on Numerical Ship Hydrodynamics, 2007.

[8] P. Peltonen, P. Kanninen, E. Laurila, V. Vuorinen, Scaling effects on the free surface backward facing step flow, Physics of Fluids 33 (4) (2021) 042106. arXiv:https://doi.org/10.1063/5.0045520, doi:10.1063/5.0045520.
URL https://doi.org/10.1063/5.0045520

[9] E. Baba, Wave breaking resistance of ships, Mitsubishi Heavy Industries Ltd, Technical Bulletin No. 110 1976 (Bulletin No. 110) (1976).

[10] T. Yamano, T. Ikebuchi, I. Funeno, Stern waves consisting of forward-oriented breaking waves and the remaining following waves, Journal of Marine Science and Technology 6 (1) (2001) 13–22. doi:10.1007/s007730170003.
URL https://doi.org/10.1007/s007730170003

[11] T. Yamano, Y. Kusunoki, F. Kuratani, T. Ogawa, T. Ikebuchi, I. Funeno, A method to confirm scale effect of stern waves due to a transom

stern, Journal of the Kansai Society of Naval Architects, Japan 2002 (2002) 133–137.

[12] T.-N. Duy, T. Hino, K. Suzuki, Numerical study on stern flow fields of ship hulls with different transom configurations, Ocean Engineering 129 (2017) 401–414. doi:10.1016/j.oceaneng.2016.10.052.
URL https://doi.org/10.1016/j.oceaneng.2016.10.052

[13] Y. K. Demirel, O. Turan, A. Incecik, Predicting the effect of biofouling on ship resistance using CFD, Applied Ocean Research 62 (2017) 100–118. doi:10.1016/j.apor.2016.12.003.
URL https://doi.org/10.1016/j.apor.2016.12.003

[14] S. Song, Y. K. Demirel, C. D. M. Muscat-Fenech, T. Tezdogan, M. Atlar, Fouling effect on the resistance of different ship types, Ocean Engineering 216 (2020) 107736. doi:10.1016/j.oceaneng.2020.107736.
URL https://doi.org/10.1016/j.oceaneng.2020.107736

[15] A. Farkas, N. Degiuli, I. Martić, R. Dejhalla, Impact of hard fouling on the ship performance of different ship forms, Journal of Marine Science and Engineering 8 (10) (2020) 748. doi:10.3390/jmse8100748.
URL https://doi.org/10.3390/jmse8100748

[16] R. Pattenden, S. Turnock, N. Bressloff, The use of detached eddy simulation in ship hydrodynamics (01 2004).

[17] P. Carrica, J. Huang, R. Noack, D. Kaushik, B. Smith, F. Stern, Large-scale DES computations of the forward speed diffraction and pitch and heave problems for a surface combatant, Computers & Fluids 39 (7) (2010) 1095–1111. doi:10.1016/j.compfluid.2010.02.002.
URL https://doi.org/10.1016/j.compfluid.2010.02.002

[18] J. Wang, Z. Ren, D. Wan, Study of a container ship with breaking waves at high froude number using URANS and DDES methods, Journal of Ship Research 64 (04) (2020) 346–356. doi:10.5957/josr.09180081.
URL https://doi.org/10.5957/josr.09180081

[19] C.-H. Yin, J.-W. Wu, D.-C. Wan, Model- and full-scale vlcc resistance prediction and flow field analysis based on iddes method 31 (2016) 259–268. doi:10.16076/j.cnki.cjhd.2016.03.001.

[20] M. Boudreau, G. Dumas, J.-C. Veilleux, Assessing the ability of the DDES turbulence modeling approach to simulate the wake of a bluff body 4 (3) (2017) 41. doi:10.3390/aerospace4030041.
URL https://doi.org/10.3390/aerospace4030041

[21] W. Yuan, A. Wall, R. Lee, Combined numerical and experimental simulations of unsteady ship airwakes 172 (2018) 29–53. doi:10.1016/j.compfluid.2018.06.006.
URL https://doi.org/10.1016/j.compfluid.2018.06.006

[22] F. White, Viscous fluid flow, McGraw-Hill Higher Education, New York, NY, 2006.

[23] W. J. Kim, S. H. Van, D. H. Kim, Measurement of flows around modern commercial ship models, Experiments in Fluids 31 (5) (2001) 567–578. doi:10.1007/s003480100332.
URL https://doi.org/10.1007/s003480100332

[24] Kriso container ship (kcs), hull data and conditions, https://t2015.nmri.go.jp/kcs_gc.html, [Online; accessed 11-May-2021] (2015).
URL https://t2015.nmri.go.jp/kcs_gc.html

[25] P. R. Spalart, S. Deck, M. L. Shur, K. D. Squires, M. K. Strelets, A. Travin, A new version of detached-eddy simulation, resistant to ambiguous grid densities 20 (3) (2006) 181–195. doi:10.1007/s00162-006-0015-0.
URL https://doi.org/10.1007/s00162-006-0015-0

[26] P. Peltonen, P. Kanninen, E. Laurila, V. Vuorinen, The ghost fluid method for OpenFOAM: A comparative study in marine context, Ocean Engineering 216 (2020) 108007. doi:10.1016/j.oceaneng.2020.108007.
URL https://doi.org/10.1016/j.oceaneng.2020.108007

[27] H. G. Weller, G. Tabor, H. Jasak, C. Fureby, A tensorial approach to computational continuum mechanics using object-oriented techniques, Comput. Phys. 12 (6) (1998) 620. doi:10.1063/1.168744.
URL https://doi.org/10.1063/1.168744

[28] S. M. Damián, N. M. Nigro, An extended mixture model for the simultaneous treatment of small-scale and large-scale interfaces, International Journal for Numerical Methods in Fluids 75 (8) (2014) 547–574. doi:10.1002/fld.3906.
URL https://doi.org/10.1002/fld.3906

[29] V. Vukčević, H. Jasak, I. Gatin, Implementation of the ghost fluid method for free surface flows in polyhedral finite volume framework, Computers & Fluids 153 (2017) 1–19. doi:10.1016/j.compfluid.2017.05.003.
URL https://doi.org/10.1016/j.compfluid.2017.05.003

[30] F. R. Menter, Two-equation eddy-viscosity turbulence models for engineering applications, AIAA Journal 32 (8) (1994) 1598–1605. doi:10.2514/3.12149.
URL https://doi.org/10.2514/3.12149

[31] G. R. Hough, D. E. Ordway, The generalized actuator disk, Technical Report TAR-TR 6401, Therm Advanced Research, Inc (1964).

[32] B. Šeb, Numerical characterisation of a ship propellers, Master's thesis. Faculty of Mechanical Engineering and Naval Architecture, University of Zagreb (2017).

[33] M. P. Schultz, Effects of coating roughness and biofouling on ship resistance and powering, Biofouling 23 (5) (2007) 331–341. doi:10.1080/08927010701461974.
URL https://doi.org/10.1080/08927010701461974

[34] M. P. Schultz, Frictional resistance of antifouling coating systems, Journal of Fluids Engineering 126 (6) (2004) 1039–1047. doi:10.1115/1.1845552.
URL https://doi.org/10.1115/1.1845552

[35] P. S. Granville, Three Indirect Methods for the Drag Characterization of Arbitrarily Rough Surfaces on Flat Plates, Journal of Ship Research 31 (01) (1987) 70–77. arXiv:https://onepetro.org/JSR/article-pdf/31/01/70/2230176/sname-jsr-1987-31-1-70.pdf, doi:10.5957/jsr.1987.31.1.70.
URL https://doi.org/10.5957/jsr.1987.31.1.70

[36] C. Grigson, Drag losses of new ships caused by hull finish, Journal of Ship Research 36 (02) (1992) 182–196. doi:10.5957/jsr.1992.36.2.182.
URL https://doi.org/10.5957/jsr.1992.36.2.182

[37] I. A. Yeginbayeva, M. Atlar, An experimental investigation into the surface and hydrodynamic characteristics of marine coatings with mimicked hull roughness ranges, Biofouling 34 (9) (2018) 1001–1019. doi:10.1080/08927014.2018.1529760.
URL https://doi.org/10.1080/08927014.2018.1529760

[38] Y. K. Demirel, D. Uzun, Y. Zhang, H.-C. Fang, A. H. Day, O. Turan, Effect of barnacle fouling on ship resistance and powering, Biofouling 33 (10) (2017) 819–834, pMID: 28980835. arXiv:https://doi.org/10.1080/08927014.2017.1373279, doi:10.1080/08927014.2017.1373279.
URL https://doi.org/10.1080/08927014.2017.1373279

[39] D. Uzun, R. Ozyurt, Y. K. Demirel, O. Turan, Does the barnacle settlement pattern affect ship resistance and powering?, Applied Ocean Research 95 (2020) 102020. doi:10.1016/j.apor.2019.102020.
URL https://doi.org/10.1016/j.apor.2019.102020

[40] M. R. Raupach, R. A. Antonia, S. Rajagopalan, Rough-wall turbulent boundary layers, Applied Mechanics Reviews 44 (1) (1991) 1–25. doi:10.1115/1.3119492.
URL https://doi.org/10.1115/1.3119492

[41] K. A. Flack, M. P. Schultz, T. A. Shapiro, Experimental support for townsend's reynolds number similarity hypothesis on rough walls, Physics of Fluids 17 (3) (2005) 035102. doi:10.1063/1.1843135.
URL https://doi.org/10.1063/1.1843135

[42] O. G. Akinlade, D. J. Bergstrom, Effect of surface roughness on the coefficients of a power law for the mean velocity in a turbulent boundary layer, Journal of Turbulence 8 (2007) N18. doi:10.1080/14685240701317245.
URL https://doi.org/10.1080/14685240701317245

[43] M. P. SCHULTZ, K. A. FLACK, The rough-wall turbulent boundary layer from the hydraulically smooth to the fully rough regime, Journal of

Fluid Mechanics 580 (2007) 381–405. doi:10.1017/s0022112007005502.
URL https://doi.org/10.1017/s0022112007005502

[44] M. Vallikivi, M. Hultmark, A. J. Smits, Turbulent boundary layer statistics at very high reynolds number, Journal of Fluid Mechanics 779 (2015) 371–389. doi:10.1017/jfm.2015.273.
URL https://doi.org/10.1017/jfm.2015.273

[45] D. T. Squire, C. Morrill-Winter, N. Hutchins, M. P. Schultz, J. C. Klewicki, I. Marusic, Comparison of turbulent boundary layers over smooth and rough surfaces up to high reynolds numbers, Journal of Fluid Mechanics 795 (2016) 210–240. doi:10.1017/jfm.2016.196.
URL https://doi.org/10.1017/jfm.2016.196

[46] J. Nikuradse, J. Nikuradse, Laws of flow in rough pipes, VDI Forschungsheft (1933) 361.

[47] D. I. Pullin, N. Hutchins, D. Chung, Turbulent flow over a long flat plate with uniform roughness, Physical Review Fluids 2 (8) (Aug. 2017). doi:10.1103/physrevfluids.2.082601.
URL https://doi.org/10.1103/physrevfluids.2.082601

[48] N. Speranza, B. Kidd, M. Schultz, I. Viola, Modelling of hull roughness, Ocean Engineering 174 (2019) 31–42. doi:10.1016/j.oceaneng.2019.01.033.
URL https://doi.org/10.1016/j.oceaneng.2019.01.033

[49] S. Song, Y. K. Demirel, M. Atlar, An investigation into the effect of biofouling on the ship hydrodynamic characteristics using CFD, Ocean Engineering 175 (2019) 122–137. doi:10.1016/j.oceaneng.2019.01.056.
URL https://doi.org/10.1016/j.oceaneng.2019.01.056

[50] P. Schlatter, R. Örlü, Turbulent boundary layers at moderate reynolds numbers: inflow length and tripping effects, Journal of Fluid Mechanics 710 (2012) 5–34. doi:10.1017/jfm.2012.324.
URL https://doi.org/10.1017/jfm.2012.324

[51] A. M. Castro, P. M. Carrica, F. Stern, Full scale self-propulsion computations using discretized propeller for the KRISO container ship KCS, Computers & Fluids 51 (1) (2011) 35–47.

doi:10.1016/j.compfluid.2011.07.005.
URL https://doi.org/10.1016/j.compfluid.2011.07.005

[52] P. Spalart, Trends in turbulence treatments, American Institute of Aeronautics and Astronautics, 2000. doi:10.2514/6.2000-2306.
URL https://doi.org/10.2514/6.2000-2306

[53] B. Aupoix, P. Spalart, Extensions of the spalart–allmaras turbulence model to account for wall roughness 24 (4) (2003) 454–462. doi:10.1016/s0142-727x(03)00043-2.
URL https://doi.org/10.1016/s0142-727x(03)00043-2

[54] T. Nickels, I. Marusic, S. Hafez, N. Hutchins, M. Chong, Some predictions of the attached eddy model for a high reynolds number boundary layer, Philosophical transactions. Series A, Mathematical, physical, and engineering sciences 365 (2007) 807–22. doi:10.1098/rsta.2006.1950.

[55] L. Eça, M. Hoekstra, Evaluation of numerical error estimation based on grid refinement studies with the method of the manufactured solutions, Computers & Fluids 38 (8) (2009) 1580–1591. doi:10.1016/j.compfluid.2009.01.003.
URL https://doi.org/10.1016/j.compfluid.2009.01.003

Appendix A.

Thrust T and torque Q for the actuator disk model is calculated based on the non-dimensional thrust and torque coefficients

$$K_T = \frac{T}{\rho n^2 D^4} \quad K_Q = \frac{Q}{\rho n^2 D^5} \tag{A.1}$$

from given rotation speed n. Respectively, the rotational speed n is calculated from the advance coefficient J eq. 7.

The actuator disk model includes two propeller parameters: the propeller radius R_P and the hub radius R_H. The momentum source term implementation is based on the following formulation. The total thrust T is defined via the pressure jump Δp integrated over the disk surface

$$T = \int_S \Delta p \, dS \tag{A.2}$$

$$\Delta p = A_x r^* \sqrt{1 - r^*} \tag{A.3}$$

where the normalized radius r^* is defined as

$$r^* = \frac{r' - r'_h}{1 - r'_h} \tag{A.4}$$

with $r' = \frac{r}{R_P}$ and $r'_h = \frac{R_H}{R_P}$. On the other hand the axial term is defined as follows

$$A_x = \frac{105}{8} \frac{T}{\pi (R_P - R_H)(3R_H + 4R_P)} \tag{A.5}$$

while the torque Q is given by

$$Q = \int_V r \frac{\Delta u_t}{\Delta t} \rho \, dV \tag{A.6}$$

$$\Delta u_t = A_\theta \frac{r^* \sqrt{1 - r^*}}{r^*(1 - r^*) + r'_h} \tag{A.7}$$

where

$$A_\theta = \frac{105}{8} \frac{Q}{\rho \pi u_x R_P (R_P - R_H)(3R_H + 4R_P)} \tag{A.8}$$

Figure A.19 shows the axial and transverse velocity fields in KCS case by modelled KP505 propeller geometry and the actuator disk model. The

cases are calculated at a ship speed of 24 kn and propeller rotation speed of $11.2\frac{\text{rad}}{\text{s}}$ resulting in a propeller thrust is 2005 kN and hull total resistance of 2011 kN. In the propeller case, an unsteady simulation by fixed time step 0.001 s (0.64 deg) and AMI sliding mesh interface is used. Respectively, in the actuator disk case the LTS scheme is used and an actuator disk model with $J = 0.721$ resulting in a thrust 2063 kN. In the propeller domain there are 6.4 M cells and the actual average y^+ is 497 on the blade surface.

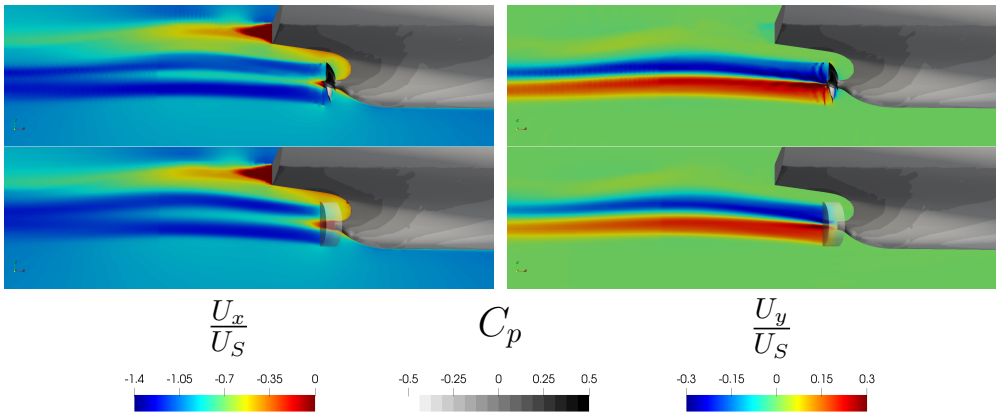

Figure A.19: The velocity distributions in the longitudinal sections $y = 0$, at right, the axial, at left transverse ($y-$direction) velocity distributions. At top, modelled propeller geometry, at down actuator disk. In the hull surface pressure coefficient $C_p = \frac{2p_d}{\rho U^2}$.

Appendix B.

OpenFOAM version v2006 rough wall function *nutURoughWallFunction* implementation is written by following a source code. The roughness Reynolds number is

$$k^+ = \frac{U_\tau k}{\nu} \tag{B.1}$$

where is roughness k, kinematic viscosity ν and friction velocity $U_\tau = \sqrt{\frac{\tau_w}{\rho}}$. Here, the wall shear stress is τ_w and the density ρ. The roughness is taken into account in the log-law region with the additional roughness function ΔU^+

$$U^+ = \frac{1}{\kappa} \ln Ey^+ - \Delta U^+ \tag{B.2}$$

where the von Kármán constant is $\kappa = 0.41$ and constant $E = 9.8$. The roughness function ΔU^+ is formulated by using a hard coded non-dimensional limit for smooth $k^+_{sm} = 2.25$ and fully rough $k^+_r = 90$ regime. C is the roughness constant and by default we set $C = 0.5$.

When $k^+ \geq k^+_r$ the ΔU^+ is

$$\Delta U^+ = \frac{1}{\kappa} \ln\left(1 + Ck^+\right) \tag{B.3}$$

and when $k^+_{sm} < k^+ < k^+_r$

$$\Delta U^+ = \frac{1}{\kappa} \ln\left(C_1 k^+ - C_2\right) sin(C_3 \ln k^+ - C_4) \tag{B.4}$$

where

$$C_1 = \frac{1}{k^+_r - k^+_{sm}} + C \tag{B.5}$$

$$C_2 = \frac{k^+_{sm}}{k^+_r - k^+_{sm}} \tag{B.6}$$

$$C_3 = \frac{\pi}{2} \frac{1}{\ln \frac{k^+_r}{k^+_{sm}}} \tag{B.7}$$

$$C_4 = \frac{\pi}{2} \frac{\ln k^+_{sm}}{\ln \frac{k^+_r}{k^+_{sm}}} \tag{B.8}$$

otherwise $\Delta U^+ = 0$.

Appendix C.

The flat plate simulation is carried out by using SST $k - \omega$ turbulence model and the results are compared to the experimental data [45]. The used rough wall model is named by *nutURoughWallFunction* in OpenFOAM-v2006. In the verification study the used roughness k (same as k_G in main text) value is 0.902 mm and the RANS model poses the same physical dimensions as the wind tunnel experiment. Total length of the model is 28 m which includes 1 m buffer ahead of the wall and the total height is 5 m. In total the 2D-model includes 1040 nodes in flow direction where 1000 is in the wall region and 200 nodes in wall normal direction where 160 nodes are located within lowest 0.5 m. Mesh refined is used towards the wall and actual

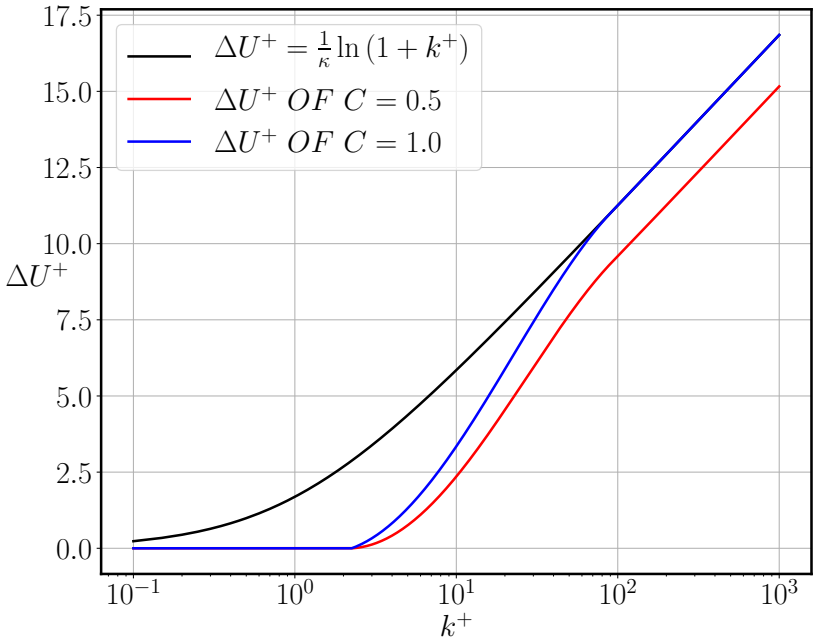

Figure B.20: Black curve Grigson roughness function [36] and OpenFOAM roughness function by roughness constant values $C = 0.5$ and 1.

y^+ average values are for smooth 99 and 134 rough case respectively. The reported background turbulence intensity for this wind tunnel is 0.05 % at 30 m/s [54]. The value is very low and causes a non-physical result using the RANS model. Here, 1 and 5 % turbulent intensity values were used at the inlet. The test is carried out with 20 and 30 m/s velocity and boundary layer thickness δ_{99} is defined by 99 % of the mean flow. The roughness function ΔU^+ value is calculated by using an equation of B.3 and B.4 depending on the roughness Reynolds number k^+.

The sensitivity for the inflow turbulence level can be seen in Table C.8 and in Figure C.21 the boundary layer thickness δ with 1 and 5 % inflow turbulent intensity is shown. In the case of 5 % inflow turbulence intensity results are closer to the reference and predict a roughness effect to the boundary layer thickness quite well. The friction velocity U_τ, roughness function value ΔU^+ and roughness Reynolds numbers are presented in Table C.8. The roughness Reynolds number is calculated in two ways, by referring to used roughness k and equivalent sand grain roughness $k_s = 1.96$ mm [45] for a comparison point of view. Authors in [45] mention a fully rough condition in the cases

where the roughness Reynolds number is nearly independent of x. Based on this study, it is possible to conclude that RANS model can predict also a fully rough condition. This can be seen by comparing cases with the same speed (20 m/s) k^+ is weakly depending on the location x in the flat plate. Fully rough condition means also that the boundary layer thickness is the only function of the location x in the flat plate i.e. does not depend on the speed.

Table C.8: Flat plate results smooth (S) and rough (R).

	S/R	x [m]	U_∞ [m/s]	δ_{99} [mm]	U_τ [m/s]	ΔU^+	k^+	k_s^+
Ref.[45]	S	21.7	30.0	278	0.93			
tu. 1 %	S	21.7	30.0	225	0.93			
tu. 5 %	S	21.7	30.0	284	0.94			
Ref.[45]	R	15	30.6	285	1.27	8.7		155
tu. 1 %	R	15	30.0	236	1.23	8.6	70	151
tu. 5 %	R	15	30.0	268	1.25	8.7	71	152
Ref.[45]	R	21.7	30.4	388	1.23	8.6		150
tu. 1 %	R	21.7	30.0	323	1.19	8.6	67	146
tu. 5 %	R	21.7	30.0	359	1.20	8.6	68	148
Ref.[45]	R	1.6	20.4	54	1.01	8.2		125
tu. 5 %	R	1.6	20.0	48	1.05	8.2	59	129
Ref.[45]	R	10	20.3	203	0.88	7.8		109
tu. 5 %	R	10	20.0	202	0.86	7.6	49	106
Ref.[45]	R	21.7	20.6	387	0.83	7.5		102
tu. 5 %	R	21.7	20.0	369	0.80	7.3	45	98

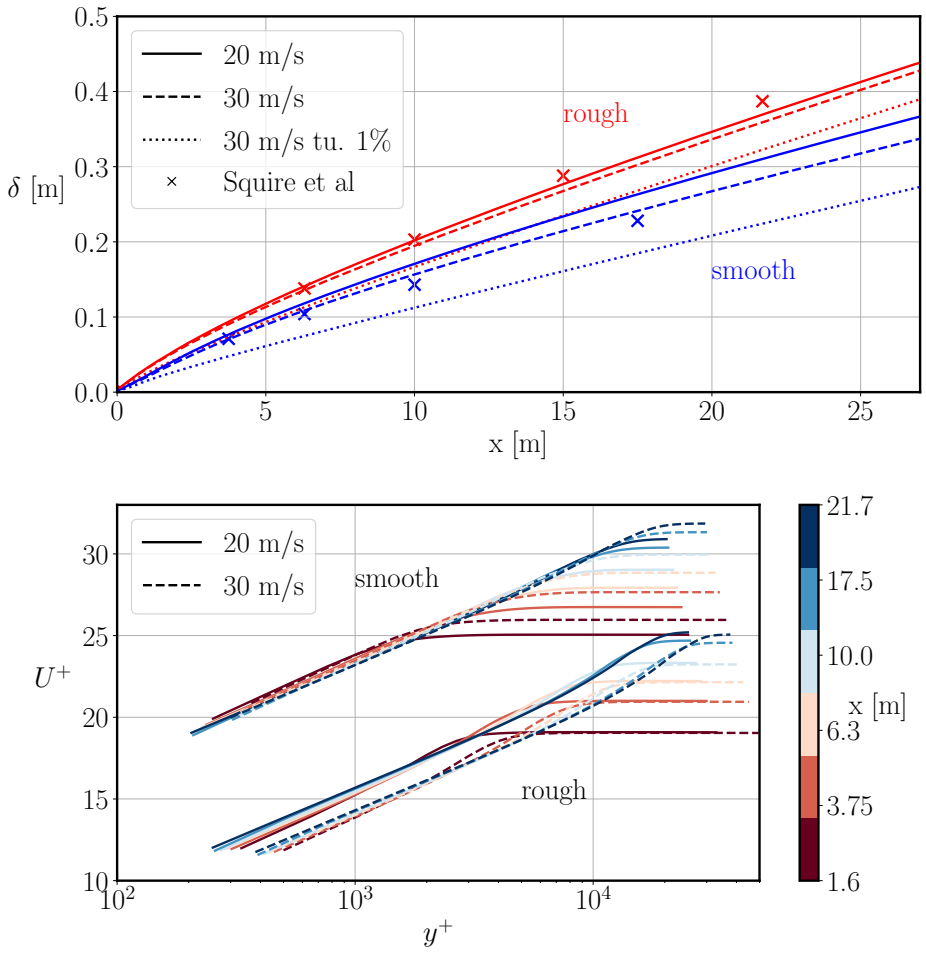

Figure C.21: The boundary layer thickness in smooth and rough flat plate case. All results from 5 % turbulent intensity inflow case unless otherwise stated.

Appendix D.

The numerical uncertainty can be divided to three different components: round-off, iterative and discretization error. The round-off error to be negligible. By refining the mesh the discretization error decreases but this requires a simulation with the multiple mesh resolution and it is not feasible in this study. The non-linearity of the solved equations cause the iterative error and it is possible to estimate it by varying convergence tolerance. The aim of the study is to investigate the iterative error by the same mesh resolution. The iterative convergence study is carried out with the case S with RANS solution by following the pressure resistance C_P. The used method follows a similar procedure as presented in [55]. The used convergence criteria for the PIMPLE loop are $c_{it} : 10^{-4}$ to 10^{-8} with one magnitude intervals, the reference level is taken from 10^{-8} results. In the PIMPLE loop the momentum and pressure equation are solved within on a time step and the tolerance affects how many loops are needed to reach the convergence criteria. The dynamic pressure p_d convergence criteria is varied and the other fields' tolerances are kept the same. Only the pressure field tolerance study is feasible because in the used method the velocity equation is not solved directly. In an OpenFOAM context this means that the *momentumPredictor* is not in use.

Case S the iterative error in the pressure resistance is 9.4 % which means 3.2 % in the total resistance, see Table D.9. The iterative tolerance effect to the stern wave shape and velocity profile is marginal, see Figure D.22. Only the case 10^{-4} show a lower wave height and the cases with tighter tolerance stern wave is slightly steeper. All cases predict separated stern wave and the transom stays dry. We can conclude that the used accuracy in case S is enough to stern wave phenomena investigation.

Table D.9: Convergence study results.

case	$C_P \times 10^3$	$C_F \times 10^3$	C_P diff. [%]
S	0.7055	1.5647	-9.4
10^{-4}	0.6097	1.5388	-21.7
10^{-5}	0.7150	1.5542	-8.2
10^{-6}	0.7275	1.5538	-6.6
10^{-7}	0.7630	1.5640	-2.0
10^{-8}	0.7787	1.5676	ref.

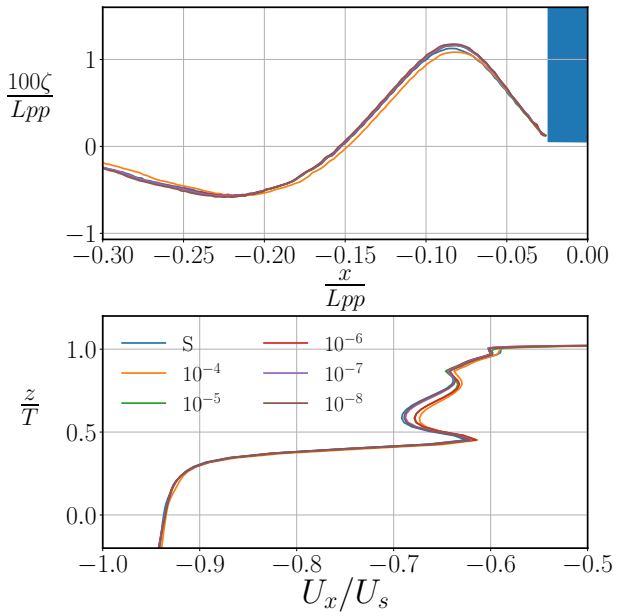

Figure D.22: Top stern wave elevation ζ and bottom velocity profile from the transom corner to downward with different iterative tolerance. Blue box represents ship transom.